Environmental Science Nano

PAPER

Cite this: *Environ. Sci.: Nano*, 2017, 4, 1494

Plasmonic resonance excited dual Z-scheme $BiVO_4/Ag/Cu_2O$ nanocomposite: synthesis and mechanism for enhanced photocatalytic performance in recalcitrant antibiotic degradation

Yaocheng Deng,[ab] Lin Tang,[*ab] Guangming Zeng,[*ab] Chengyang Feng,[ab] Haoran Dong,[ab] Jiajia Wang,[ab] Haopeng Feng,[ab] Yani Liu,[ab] Yaoyu Zhou[c] and Ya Pang[d]

The utilization of solar energy based on semiconductor photocatalysts for pollutant removal and environmental remediation has become a research hot spot and attracted great attention. In this study, a novel ternary $BiVO_4/Ag/Cu_2O$ nanocomposite has been successfully synthesized *via* simple wet impregnation of Cu_2O particles coupled with a subsequent photo-reduction pathway for the deposition of metallic Ag on the surface of $BiVO_4$. The resulting $BiVO_4/Ag/Cu_2O$ photocatalyst was used for the degradation of tetracycline (TC) under visible light irradiation ($\lambda > 420$ nm). Results showed that the coating contents of the Cu_2O and Ag particles presented a great effect on the eventual photocatalytic activity of the photocatalysts, and the optimum coating contents of Cu_2O and Ag were obtained with their mass ratios of 3% and 2%, respectively. Under optimum conditions, nearly 91.22% TC removal efficiency was obtained based on ternary $BiVO_4/Ag/Cu_2O$ nanocomposites, higher than that of pure $BiVO_4$ (42.9%) and binary $BiVO_4/Cu_2O$ (65.17%) and $BiVO_4/Ag$ (72.63%) nanocomposites. Meanwhile, the enhanced total organic carbon (TOC) removal efficiency also indicated the excellent photocatalytic degradation ability of the $BiVO_4/Ag/Cu_2O$ nanocomposites. As for their practical application, the effects of initial TC concentration, various supporting electrolytes and different irradiation conditions were investigated in detail. Three-dimensional excitation–emission matrix fluorescence spectroscopy (3D EEMs) was used to show the by-products of TC molecule degradation. Cycling experiments indicated the high stability of the as-prepared photocatalysts. Furthermore, the results obtained from radical trapping experiments and ESR measurements suggested that the photocatalytic degradation of TC in the $BiVO_4/Ag/Cu_2O$ based photocatalytic system was the joint action of the photogenerated holes (h^+), superoxide radical ($^{\bullet}O_2^-$) and hydroxyl radical ($^{\bullet}OH$). The enhanced photocatalytic activity of $BiVO_4/Ag/Cu_2O$ was attributed to the synergistic effect of Cu_2O, Ag and $BiVO_4$, especially the surface plasmon resonance effect and the established local electric field brought about by metallic Ag. Additionally, to deeply understand the reaction mechanism, a dual Z-scheme charge transfer pathway has been proposed.

Received 16th March 2017,
Accepted 9th May 2017

DOI: 10.1039/c7en00237h

rsc.li/es-nano

Environmental significance

Constructing highly efficient photocatalysts is essential for the photodegradation of environmental pollutants. In this study, we applied the surface plasmon resonance effect of metallic Ag to the $BiVO_4/Cu_2O$ composite to design a novel dual Z-scheme $BiVO_4/Ag/Cu_2O$ photocatalyst. The prepared photocatalyst displayed both promoted transfer ability and strong redox ability of the photogenerated electron–holes. The prepared $BiVO_4/Ag/Cu_2O$ photocatalyst presented high photocatalytic activity for tetracycline (TC) degradation. The reaction conditions have been systematically studied. Then, 3D EEMS was used to present the change of some intermediate products in the reaction process. Eventually, a dual Z-scheme photogenerated electron transfer mechanism has been proposed to help fully understand the reaction process among the metallic Ag, Cu_2O and $BiVO_4$. This strategy provides a new insight into the design of effective photocatalysts for environmental pollutant removal in practical application.

[a] *College of Environmental Science and Engineering, Hunan University, Changsha, 410082, China. E-mail: tanglin@hnu.edu.cn, zgming@hnu.edu.cn; Fax: +86 731 88823701; Tel: +86 731 88822778*
[b] *Key Laboratory of Environmental Biology and Pollution Control, Hunan University, Ministry of Education, Changsha 410082, China*
[c] *College of Resources and Environment, Hunan Agricultural University, Changsha 410128, China*
[d] *Department of Biotechnology and Environmental Science, Changsha College, Changsha 410003, China*

1. Introduction

Nowadays, antibiotics, as one of the largest products and applications of drugs, have been widely used for the treatment of bacterial infection all over the world.[1–5] However, owing to their continuous input and accumulation in the eco-system, they are now causing serious threats to human health. Besides, these antibiotics cannot be efficiently decomposed by traditional wastewater treatment methods due to the inhibition of the proliferation of bacteria.[6–8] Thus antibiotics have become a recalcitrant pollutant in our environment, and it is urgently needed to find an effective strategy for their removal.

In recent years, photocatalytic degradation of pollutants based on semiconductors has attracted considerable interest.[9–18] In order to effectively utilize visible light (45% in the solar spectrum energy), many visible light induced semiconductors, such as WO_3, g-C_3N_4, $BiVO_4$, Fe_2O_3, Bi_2WO_6, Cu_2O and BiOCl, have been studied and served as photocatalysts for pollutant degradation.[19–26] Monoclinic bismuth vanadate ($BiVO_4$) has attracted considerable interest as a candidate for a proper photocatalyst for pollutant degradation due to its relatively narrow band gap (2.4 eV), high chemical stability, sufficient photocatalytic activity and energy conversion.[27] Nonetheless, the rapid recombination and fast decay of photogenerated holes and electrons greatly inhibit its application in practical photocatalysis. In recent years, the design of hybrid or multicomponent photocatalysts with the formation of a heterojunction, p–n junction or Schottky junction, has been demonstrated as a strategy in hindering the recombination of photogenerated electrons and holes *via* an efficient charge transport process, possessing strong redox ability at spatially separate sites. Based on the principle mentioned above, Cu_2O was used as another semiconductor to combine with $BiVO_4$ to efficiently promote the performance of $BiVO_4$ with the formation of a p–n heterojunction due to the match of their band gaps.[10,28,29] However, it is known that the electrons or holes display weaker redox ability during the transfer process. Thus, an unavoidable problem of traditional semiconductor heterojunction is that the redox abilities of transferred electrons and holes are reduced, which brings about a negative effect on the photocatalytic reaction process.[30,31] Therefore, a more efficient strategy for the design of a photocatalytic reaction system that can bring about both fast photogenerated charge transfer efficiency and strong redox ability is needed.

In the past decade, the Z-scheme charge transfer mechanism has been proposed and investigated as a new charge transfer type for the description of reaction processes. Different from the traditional charge transfer type, such a Z-scheme charge transfer pathway not only can greatly promote the photogenerated charge separation efficiency but also can preserve the strong redox ability of the photogenerated electrons and holes.[30,32,33] So far, a lot of Z-scheme photocatalytic systems have been reported, such as Ag_2CrO_4/g-C_3N_4, CdS/WO_3, and α-Fe_2O_3/Cu_2O,[19,34,35] presenting much better photocatalytic abilities than single photocatalysts. Nonetheless, in some semiconductor heterojunctions, the coexisting typical charge transfer competes with the Z-scheme charge transfer process. For this reason, an electron mediator that serves as a contact interface or a conductor with low contact resistance is needed for accelerating the photogenerated electron–hole pair transfer.[36] For example, in our previous study, Bi metal was used as the electron mediator to promote the photocatalytic activity of g-C_3N_4 and Bi_2WO_6 nanocomposite.[37]

Additionally, in many Z-scheme systems, Ag has been used as a mediator for its excellent electron conductivity.[38–40] Owing to the existence of surface plasmon resonance (SPR) and its induced local electric field, Ag can also enhance the absorption of visible light and boost the photogenerated electron transfer. For instance, Zhu and co-authors proposed that the existence of Ag nanoparticles in hybrid Ag/Fe_3O_4/g-C_3N_4 photocatalyst can improve the visible light absorption ability and greatly enhance the photocatalytic performance.[41] However, most of the time, the metallic Ag nanoparticle was just treated as an electron mediator, and the electron transfer pathways in the inner Ag metal were not presented clearly. To solve this problem, Yu and co-authors pointed out that a dual Z-scheme charge transfer mechanism would exist in the prepared TiO_2–Ag–Cu_2O composite and show enhanced photocatalytic hydrogen generation. This explanation was more reasonable for the Ag based composite and indicated that the introduction of a surface plasmon resonance effect into the nanocomposite helps to design high performance dual Z-scheme photocatalysts.[32]

In this study, we rationally applied the surface plasmon resonance effect of metallic Ag on the $BiVO_4$/Cu_2O nanocomposite to design a dual Z-scheme $BiVO_4$/Ag/Cu_2O photocatalyst. Among the photocatalysts, Cu_2O nanoparticles were loaded onto the $BiVO_4$ surface *via* a wet-impregnation method followed by the deposition of Ag onto the photocatalyst *via* a facile photodeposition method. Tetracycline (TC), a typical antibiotic, was chosen as a target recalcitrant pollutant to explore the photocatalytic performance. Results showed that the amount of both Cu_2O and Ag showed an important influence on the photocatalyst activity. Furthermore, a tentative mechanism analysis showed that both $BiVO_4$ and Cu_2O could be excited under visible light irradiation. Then owing to the formation of a Schottky barrier on the Ag and $BiVO_4$ interface, the photogenerated electrons in the conductor band (CB) of $BiVO_4$ would migrate to Ag. Simultaneously, the excited electrons produced in Ag due to the existence of the SPR-induced local electric field will combine with holes on the valence band (VB) of Cu_2O. Eventually, based on the active species trapping experiment results and electron spin resonance (ESR) analysis, a dual Z-scheme photogenerated electron transfer mechanism has been proposed.

2. Experimental section

2.1. Materials

Bismuth nitrate hexahydrate ($Bi(NO_3)_3{\cdot}5H_2O$), ammonium vanadate (NH_4VO_3), cupric acetate ($Cu(CH_3COO)_2{\cdot}H_2O$), di-

ethylene glycol (DEG) and tetracycline were purchased from Sinopharm Chemical Regent Co. Ltd (Shanghai, China). All chemicals used in this work were of analytical grade and used without further purification. Solutions were freshly prepared with deionized water.

2.2. Preparation of monoclinic bismuth vanadate ($BiVO_4$)

Monoclinic bismuth vanadate ($BiVO_4$) was prepared by a hydrothermal method as reported in the literature.[21,22] Briefly, 36 mmol of NH_4VO_3 and 36 mmol of $Bi(NO_3)_3{\cdot}5H_2O$ were separately dissolved in 150 ml of 2 M nitric acid solutions. Then the above solutions were mixed to form a yellow homogeneous solution. The pH value of the resulting homogeneous solution was adjusted to approximately 2.0 with ammonia solution. During the adjustment of the pH value of the solution, a yellow precipitate was produced at the bottom and the solution was kept stirring for another 30 min. After aging for 2 h, the yellow precipitate at the bottom of the beaker was transferred to a 100 mL Teflon-lined stainless steel autoclave and accounted for 70% volume of the autoclave. The autoclave was heated to 200 °C and maintained at this temperature for 24 h. After cooling to room temperature, a yellow powder was collected by filtration and then washed several times with distilled water. Finally, the obtained sample was dried at 60 °C for 10 h.

2.3. Preparation of $BiVO_4/Cu_2O$ nanocomposites

Cu_2O nanoparticles were loaded on the surface of $BiVO_4$ nanoparticles by a wet impregnation method. Typically, a certain amount of $Cu(CH_3COO)_2{\cdot}H_2O$ was dissolved in 50 mL of ethanol; 300 mg $BiVO_4$ was subsequently added to the solution and ultrasonically treated to form a suspension mixture. Then the mixture was kept stirring for 10 h and dried to obtain the powder mixture of $Cu(CH_3COO)_2{\cdot}H_2O$ and $BiVO_4$. Next, the obtained powder mixture was suspended in 150 mL of DEG solution, transferred to a flask and heated at 180 °C for 2 h with constant stirring at a speed of 500 rpm. The solid product was collected by filtration, washed with ethanol and water repeatedly, and dried at 80 °C in a vacuum oven for 12 h. The as-prepared samples were labeled $BiVO_4$/1%Cu_2O, $BiVO_4$/2%Cu_2O, $BiVO_4$/3%Cu_2O, $BiVO_4$/4%Cu_2O and $BiVO_4$/5%Cu_2O when the mass ratios of Cu_2O : $BiVO_4$ were 1%, 2%, 3%, 4% and 5%, respectively.

2.4. Preparation of $BiVO_4/Ag/Cu_2O$ nanocomposites

$BiVO_4/Ag/Cu_2O$ nanocomposite was achieved *via* a photoreduction procedure. Typically, 0.3 g of the prepared $BiVO_4/Cu_2O$ nanocomposite and a certain amount of $AgNO_3$ were added into 20 ml methanol solution (containing 4 ml methanol). Subsequently, the mixture solution was treated with irradiation from a 300 W Xe lamp for 2 h. After that, the suspension was collected by filtration and thoroughly washed with ethanol and deionized water several times to remove the residual impurity. Then the sample was dried at 60 °C in a vacuum oven for 12 h. The prepared samples were labeled x $BiVO_4/Ag/Cu_2O$ (x represents the mass ratio of Ag to the samples, and x = 1%, 1.5%, 2%, 2.5% and 3%). For comparison, $BiVO_4$/2% Ag was also prepared *via* the same procedure using pure $BiVO_4$ nanoparticles. In addition, to make the description more clear, in the following experiment $BiVO_4/Cu_2O$ and $BiVO_4/Ag/Cu_2O$ were used to represent the optimum $BiVO_4$/3%Cu_2O and $BiVO_4$/2%Ag/3%Cu_2O samples, respectively.

2.5. Characterization

X-ray diffraction (XRD) pattern measurements of the prepared samples were undertaken using a Bruker AXS D8 Advance system with a Cu Kα irradiation source at a scan rate (2θ) of 0.05° s^{-1}. The morphology of the as-prepared samples was investigated by scanning electron microscopy (SEM) using a Hitachi S-4800 field emission scanning electron microscope (FE-SEM Hitachi, Japan) with 5.0 kV scanning voltages. Transmission electron microscopy (TEM), high-resolution transmission electron microscopy (HRTEM) and high angle angular dark field-scanning transmission electron microscopy (HAADF-STEM) images were obtained using an F20 S-TWIN electron microscope (Tecnai G2, FEI Co.) at the acceleration voltage of 200 kV. X-ray photoelectron spectroscopy (XPS) measurements of the prepared samples were obtained using a Thermo Fisher ESCALAB 250Xi spectrometer with an Al Kα source. The ultraviolet visible diffused reflectance spectra (UV-vis DRS) of the prepared samples were collected using a UV-vis spectrophotometer (Cary 300, USA) equipped with an integrating sphere, using $BaSO_4$ as the reference. The total organic carbon (TOC) assays were performed using a Shimadzu TOC-VCPH analyzer. Three-dimensional excitation–emission matrix fluorescence spectra (3D EMMs) were obtained using an F-4500 spectrofluorometer with an emission wavelength range of λ_{em} = 300–550 nm and an excitation wavelength range of λ_{ex} = 200–450 nm. The electron spin resonance (ESR) signals of radicals spin-trapped using the spin-trapping reagents 5,5-dimethyl-1-pyrroline *N*-oxide (DMPO) were examined on a Bruker ER200-SRC spectrometer under visible light irradiation (λ > 420 nm).

2.6. Photocatalytic activity analysis

The photocatalytic performances of the as-prepared samples were evaluated by the degradation of TC under visible light irradiation. A 300 W Xe lamp (PLS/SXE 300C, Beijing Perfectlight Co., Ltd.) equipped with a UV cutoff filter (λ > 420 nm) was used to remove the light at a wavelength less than 420 nm. Before being exposed to light irradiation, 40 mg of the sample powder was dispersed into 100 mL of 20 mg L^{-1} TC aqueous solution. To make sure the adsorption equilibrium was reached, the suspension solution was kept stirring in the dark for 30 min before irradiation. During the illumination process, 4 mL of aqueous solution was separated and sampled from the suspended photocatalyst nanoparticles for measurement at certain time intervals. The photocatalytic degradation efficiency was measured using a

Shimadzu UV-vis spectrophotometer (UV-2550) at the characteristic absorption peak of 357 nm for TC.

2.7. Photoelectrochemical measurements

The photocurrent responses of the prepared samples were investigated in a conventional three-electrode model on a CHI 660D workstation. A Pt electrode was employed as the counter electrode and an Ag/AgCl electrode in saturated KCl solution was used as the reference electrode. The photocatalysts were coated on the FTO as the working electrode. Typically, the working electrodes were prepared as follows. 20 mg of the photocatalyst was suspended in 1 mL 0.25% Nafion solution to make a slurry. Then, 200 μL of the slurry was dropped onto a 1 cm × 2 cm FTO slice. The available surface area of the working electrode was 1.0 cm^2, and 0.2 M sodium sulfate electrolyte solution was used as an electrolyte in the photoelectrochemical test system. A 300 W Xe lamp with a UV cut-off filter was used as the visible light lamp. To further study the photoelectrochemical characteristics of the prepared samples, cathodic polarization curves were also obtained and electrochemical impedance spectroscopy (EIS) was performed. The cathodic polarization curves were collected based on the above test system using a linear sweep voltammetry (LSV) technique with a scan rate of 0.2 mV s^{-1}. EIS was performed on an Autolab workstation (AUT85812) equipped with a frequency analyzer module based on the above three-electrode system except that the electrolyte was replaced by a 0.1 M KCl solution containing 5 mM $Fe(CN)_6^{3-/4-}$.

3. Results and discussion

3.1. Structure and morphology characteristics

Fig. 1 shows the XRD patterns of the as-prepared $BiVO_4$, $BiVO_4/Cu_2O$ and $BiVO_4/Ag/Cu_2O$ nanocomposites with the optimum contents of Cu_2O and Ag. The main peaks of pure $BiVO_4$ nanoparticles can be observed, such as (110), (011), (121), (040), (200), (002), (211), (150), (132), (240), (042), (−202), (161), (170) and (321), belonging to the crystal planes of monoclinic $BiVO_4$ (JCPDS No. 14-0668).[29] The XRD patterns of the as-prepared $BiVO_4/Cu_2O$ and $BiVO_4/Ag/Cu_2O$ are quite similar to those of the as-prepared pure $BiVO_4$ particles. It should be noted that no obvious peaks of copper oxide or silver can be detected, which is due to the low loading amount, small particle size, good dispersion and the dominant peaks of $BiVO_4$ in the prepared nanocomposites. This result also indicated that the pristine crystal structure of $BiVO_4$ cannot be destroyed during the coating process of Cu_2O and Ag particles, which is important for the high photocatalytic performance of the ternary $BiVO_4/Ag/Cu_2O$ nanocomposite in the photocatalytic degradation experiments. Meanwhile, there are no additional crystal phases in all the patterns, indicating no impurity was produced in the preparation process.

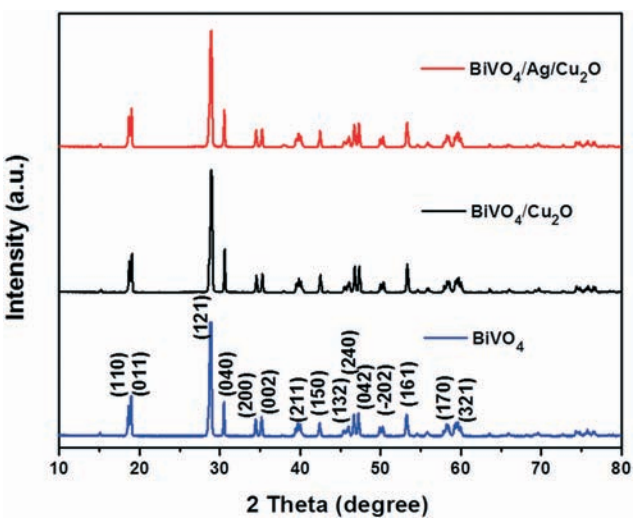

Fig. 1 XRD patterns of the prepared $BiVO_4$, $BiVO_4/Cu_2O$ and $BiVO_4/Ag/Cu_2O$ nanocomposites.

The morphology of the prepared samples was characterized by SEM. As shown in Fig. 2a and b, the as-prepared pure $BiVO_4$ nanoparticles present an approximately cubic structure with a smooth surface. These nanoparticles exhibit a wide size distribution from about 1 to 5 μm.[21,22] Fig. 2c and d show the SEM images of the as-prepared $BiVO_4/Cu_2O$ nanocomposites with different magnifications. It can be seen that there are many Cu_2O nanoparticles coated on the surface of the $BiVO_4$ nanoparticles. Compared to pure $BiVO_4$, the surface of the prepared $BiVO_4/Ag/Cu_2O$ nanocomposites was not smooth any more but was rough instead due to the coating of Ag and Cu_2O nanoparticles, which could increase the reaction surface of the samples and provide more active sites, resulting in enhanced photocatalytic activity and performance (Fig. 2e and f). To study the detailed morphology characterization of the prepared $BiVO_4$ and $BiVO_4/Ag/Cu_2O$ nanocomposites, TEM images are provided in Fig. 3. Similar to the results from the SEM image, the surface of $BiVO_4$ was smooth (Fig. 3a), but for $BiVO_4/Ag/Cu_2O$, some obvious Ag and Cu_2O nanoparticles were coated on the surface of $BiVO_4$ (Fig. 3b–d). HRTEM of $BiVO_4/Ag/Cu_2O$ has been further studied and results are provided in Fig. 3e. The region of the HRTEM was at the edge of the big particle of $BiVO_4$ marked in Fig. 3c and d. In Fig. 3e, we can see that at the edge of the $BiVO_4$, the crystal lattice space was 0.308 nm, corresponding to the (121) plane of $BiVO_4$. Then on the surface of $BiVO_4$, many nanoparticles exist. According to the analysis results of the relative crystal lattice space, in the place close to $BiVO_4$, a lattice space of 0.237 nm exists, which refers to the (111) plane of Ag, and then a little far away from the $BiVO_4$, the crystal lattice space of 0.241 nm belongs to the (111) plane of Cu_2O. The results demonstrate the co-existence of both Ag and Cu_2O and the intimate contact of Ag and Cu_2O on the surface of $BiVO_4$ particles. Furthermore, to demonstrate the element properties and the homogeneous distribution of the nanoparticles, a HAADF STEM image and the corresponding EDS mapping

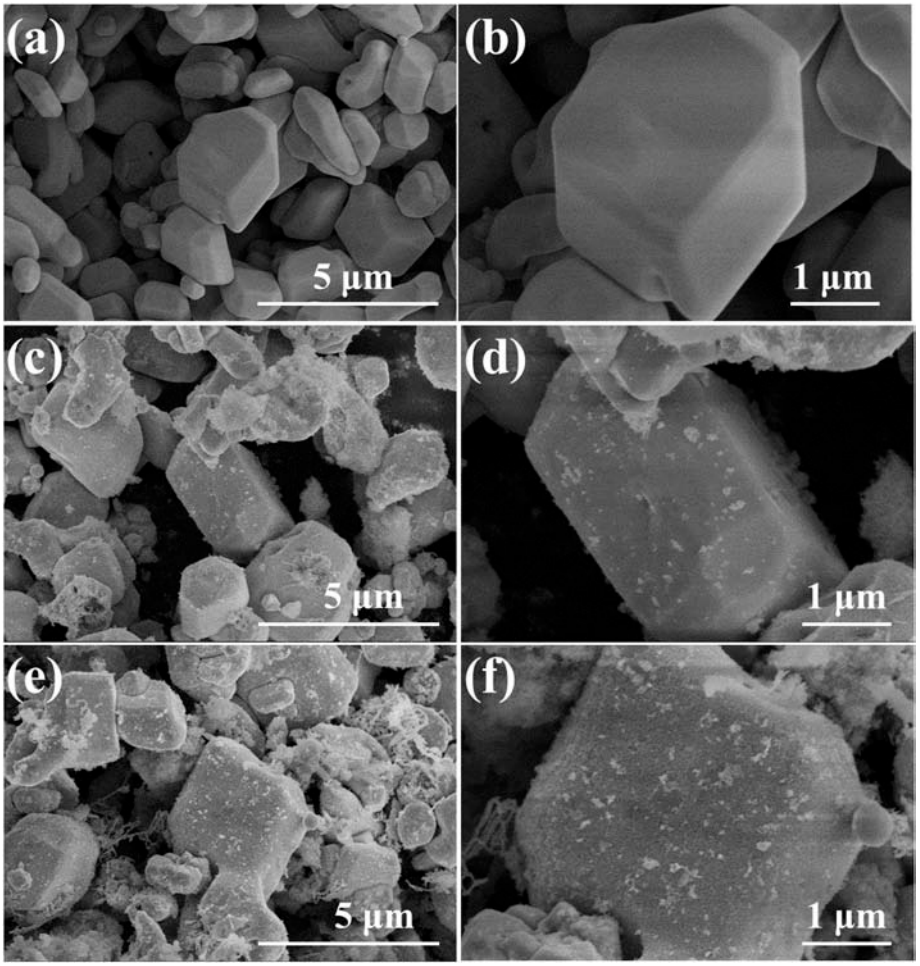

Fig. 2 SEM images of (a and b) $BiVO_4$, (c and d) binary $BiVO_4/Cu_2O$ nanocomposites and (e and f) ternary $BiVO_4/Ag/Cu_2O$ composites.

image marked by a red box in Fig. 3f are provided (Fig. 3g and l). We can see that the existence of Bi, V, O, Cu and Ag elements and the good distribution of these elements indicate the homogeneous coverage of Ag and Cu_2O nanoparticles on the surface of $BiVO_4$.

3.2. Specific surface area and surface chemical composition analysis

To demonstrate the increased specific surface of the prepared $BiVO_4/Ag/Cu_2O$ nanocomposite due to the coating of Ag and Cu_2O on the surface of $BiVO_4$, N_2 adsorption–desorption of $BiVO_4$ and $BiVO_4/Ag/Cu_2O$ nanocomposite was studied, as shown in Fig. 4. After calculating the obtained data, the BET specific surface areas of the prepared $BiVO_4$ and $BiVO_4/Ag/Cu_2O$ nanocomposite were 17.05 and 22.78 $m^2\ g^{-1}$, respectively, and the relative pore volumes of $BiVO_4$ and $BiVO_4/Ag/Cu_2O$ samples were 0.02 and 0.05 $cm^3\ g^{-1}$, respectively. The results demonstrate that the coating of Ag and Cu_2O nanoparticles on the surface of the $BiVO_4$ can increase the specific surface area of the prepared $BiVO_4/Ag/Cu_2O$ nanocomposite, indicating that more reaction sites can be provided and the photocatalytic activity of the prepared samples will be promoted.

The binding states and the elemental compositions of the prepared $BiVO_4/Ag/Cu_2O$ nanocomposite have been studied *via* survey XPS analysis of all elements and high-resolution XPS study for the Bi 4f, V 2p, O 1s, Cu 2p, and Ag 3d. As shown in Fig. 5a, the survey XPS spectrum of $BiVO_4/Ag/Cu_2O$ shows that the main elements of the prepared samples are Bi, V, O, Cu, Ag and a trace amount of C. The peaks of the C elements might belong to adventitious hydrocarbon that exists in the XPS instrument.[42] Fig. 5b shows the high-resolution spectra of C 1s, and the peak located at 284.6 eV is used to correct the instrument error for accurate analysis. Fig. 5c–g present the high resolution spectra of Bi 4f, V 2p, O 1s, Cu 2p, and Ag 3d for the $BiVO_4/Ag/Cu_2O$ composite, respectively. As shown in Fig. 5c, the peaks located at 158.5 eV and 163.7 eV belong to the binding energy of Bi $4f_{7/2}$ and Bi $4f_{5/2}$, respectively. As for V 2p (Fig. 5d), the main peak at 516.1 eV refers to V $2p_{3/2}$, and another relatively small peak at 523.4 eV should be V $2p_{1/2}$.[42,43] The high-resolution spectra of O 1s can be divided into three peaks, and the two main peaks located at 529.3 eV and 530.7 eV correspond to the oxygen species of the lattice oxygen of layer-structured $Bi_2O_2^{2+}$ and Cu_2O, respectively. Another small peak with the binding energy of 531.3 eV may come from the surface hydroxyl group

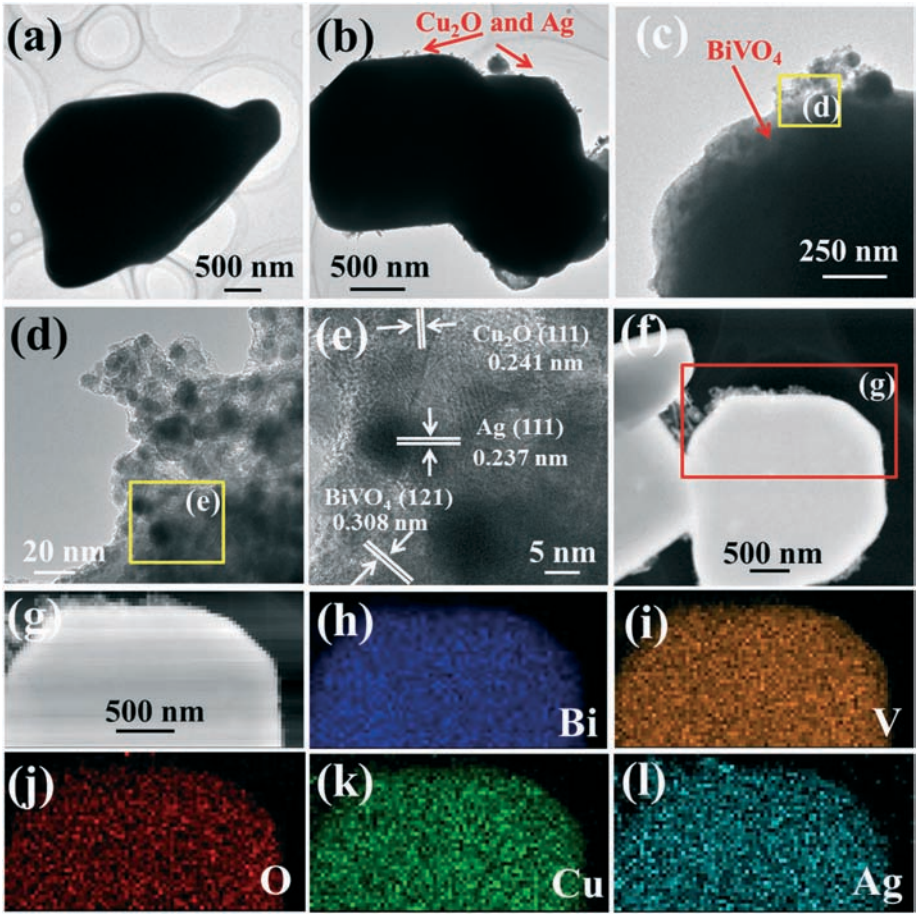

Fig. 3 TEM image of (a) $BiVO_4$ and (b–d) $BiVO_4/Ag/Cu_2O$ nanocomposites. (e) HRTEM image of the prepared $BiVO_4/Ag/Cu_2O$. (f–g) HAADF-STEM image of $BiVO_4/Ag/Cu_2O$. (h–l) The corresponding EDS mapping images of Bi, V, O, Cu and Ag elements in the red box area.

or the adsorbed H_2O on the surface of the samples (Fig. 5e).[44] Fig. 5f displays the main and the satellite peaks of Cu $2p_{3/2}$ and Cu $2p_{1/2}$ core levels of the $BiVO_4/Ag/Cu_2O$ sample. It has been reported that copper oxide can exist in two semiconducting phases, namely, CuO and Cu_2O. Two peaks located at 951.7 eV and 931.8 eV are clearly found, corresponding to Cu $2p_{1/2}$ and Cu $2p_{3/2}$ bands of Cu_2O crystallites, respectively. Three other peaks located at 933.9 eV, 942.3 eV and 954.3 eV are also found. The main peak in the XPS spectrum of the Cu 2p band is known to be characteristic of Cu^+, and the other three additional peaks could belong to the Cu^{2+} state, which indicates the existence of CuO.[28,42] It should be noted that the loading method to prepare the $BiVO_4/Ag/Cu_2O$ photocatalysts is a wet impregnation process, not a simple and direct mixing process. Thus the production of CuO peaks is probably due to the partial surface oxidation of Cu_2O nanoparticles during the preparation process. However, this phenomenon cannot change the fact that the main existing state of the Cu element is Cu^+. In the high-resolution XPS spectra of Ag 3d shown in Fig. 5g, the two main peaks observed at 368.3 eV and 374.1 eV can be assigned to metal Ag species.[9]

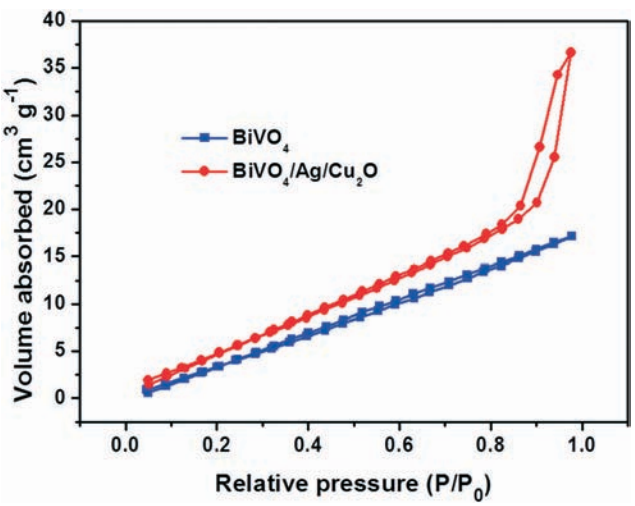

Fig. 4 N_2 absorption–desorption spectra of the prepared $BiVO_4$ and $BiVO_4/Ag/Cu_2O$ composites.

3.3. Optical properties

The UV-vis diffuse reflectance spectra of the prepared samples are displayed in Fig. 6a. Among all the samples, the absorption edges of pure $BiVO_4$ are determined to be ~550 nm,

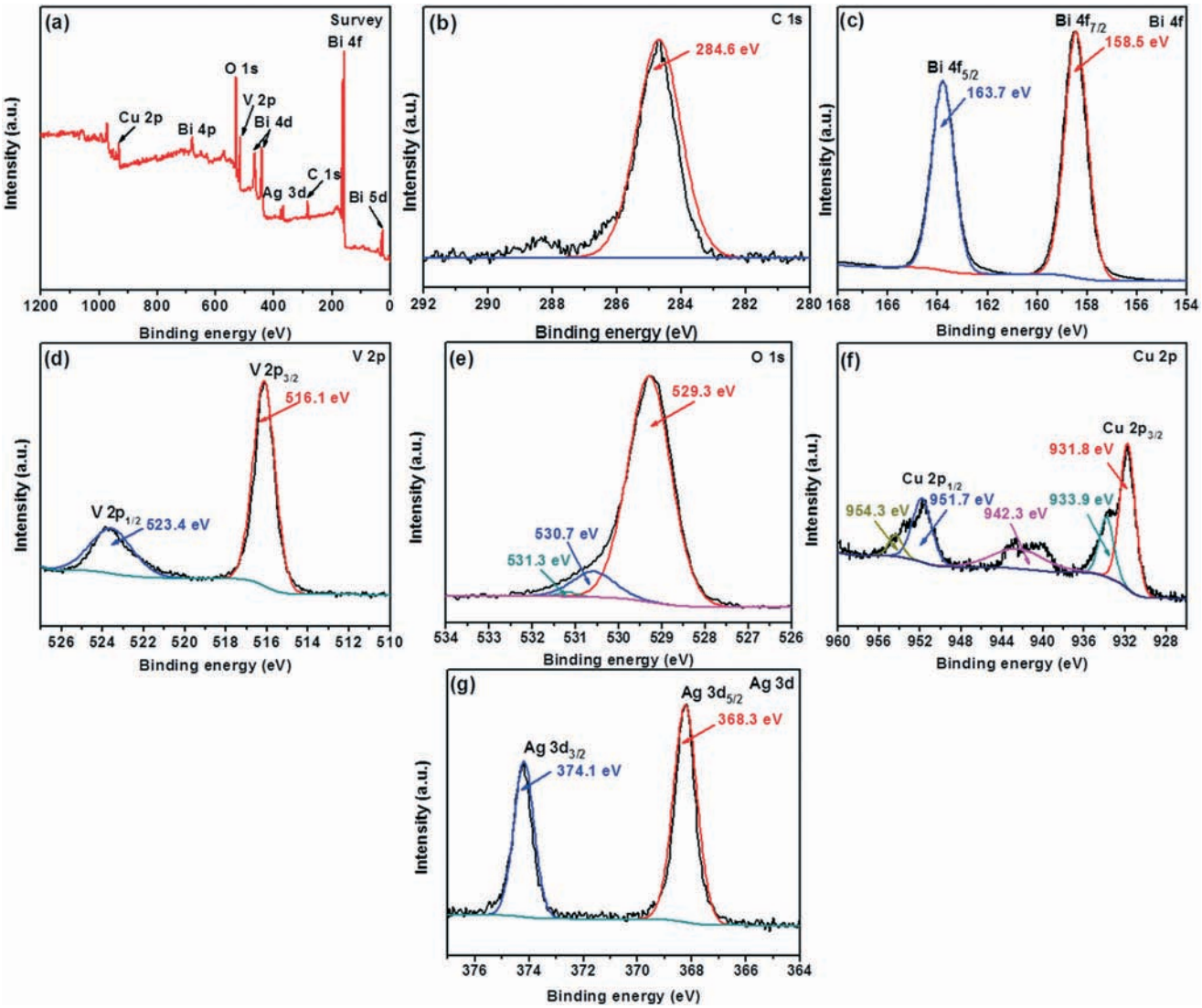

Fig. 5 The XPS spectra of $BiVO_4$/Ag/Cu_2O nanocomposites: (a) survey spectra, (b–g) high-resolution spectra of C 1s, Bi 4f, V 2p, O 1s, Cu 2p and Ag 3d, respectively.

which is in accordance with previous reports.[45,46] In particular, when Cu_2O or Ag was coated on the surface of the $BiVO_4$, the $BiVO_4$/Cu_2O and $BiVO_4$/Ag samples presented an enhanced light absorption compared to the pristine $BiVO_4$ in the whole visible range of 400–800 nm. In particular, $BiVO_4$/Ag/Cu_2O shows remarkable absorption ability in visible light compared to the other three samples. Moreover, the broad absorption bands of the prepared $BiVO_4$/Ag and $BiVO_4$/Ag/Cu_2O nanocomposites in the visible light region are ascribed to the SPR absorption of Ag nanoparticles. The SPR effect of metallic Ag makes the transfer of energy among the prepared $BiVO_4$/Ag/Cu_2O composites mainly due to the following three ways: (i) making the absorption wavelength region red shift; (ii) making the surface of $BiVO_4$ become rough due to the coating of metallic Ag, which could the increase light scattering effect; (iii) transferring the plasmon energy from the metal to the semiconductor, which can help to induce the photogeneration of electrons and holes. This result implies that the coating of Ag and Cu_2O can improve the visible-light absorption ability and may tend to improve the photocatalytic activity.

To deeply understand the band gap of the prepared samples, the relative band gap of the prepared samples was calculated by the following formula:

$$\alpha h\nu = A(h\nu - E_g)^{n/2} \quad (1)$$

where α, h, ν, E_g, and A are the absorption coefficient, Planck constant, light frequency, band gap energy, and a constant, respectively. Among them, n is determined by the type of optical transition of a semiconductor (n = 1 for direct transition, and n = 4 for indirect transition). From the plot of $(\alpha h\nu)^2$

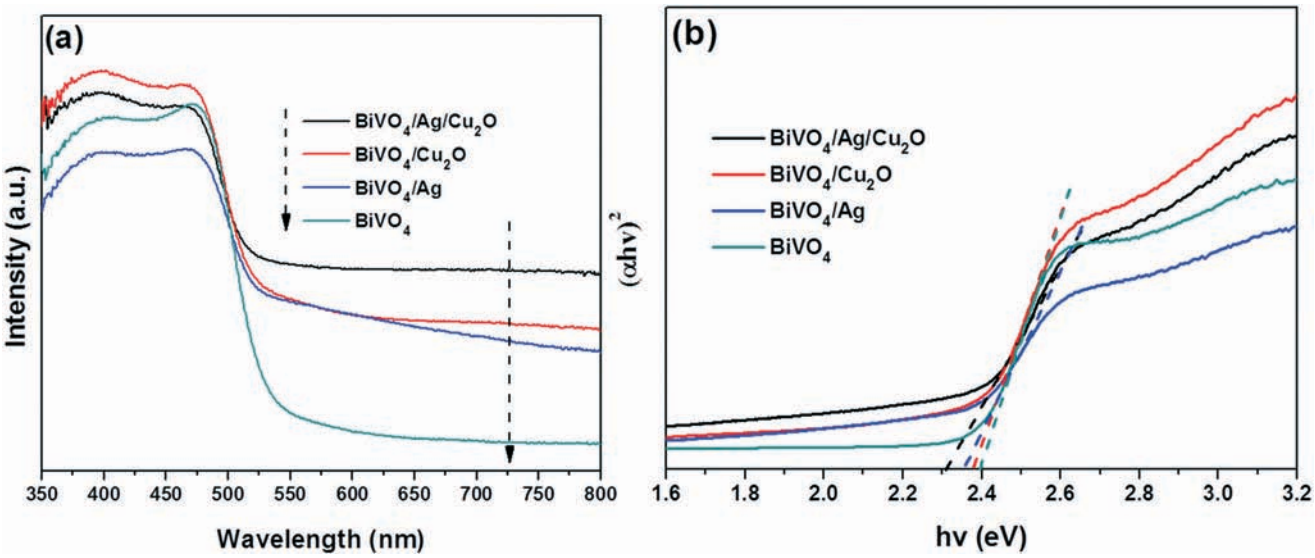

Fig. 6 (a) UV-vis diffuse reflectance spectra and (b) the relative band gap energy of the prepared samples.

versus ($h\nu$) in Fig. 6b, the E_g values of $BiVO_4$, $BiVO_4/Cu_2O$, $BiVO_4/Ag$ and $BiVO_4/Ag/Cu_2O$ are estimated to be 2.40, 2.37, 2.35 and 2.31 eV, respectively. The coating of Ag and Cu_2O on the surface of $BiVO_4$ results in changes in the band gap of the prepared hybrid composites and makes the band gap become narrower, which leads to enhanced visible light response ability and broadened light response edge of the prepared samples.

3.4. Photoluminescence and photoelectrochemical analysis

Photoluminescence (PL) spectroscopy has been widely employed to study the photogenerated charge carrier excitation and transfer in photocatalysis over a semiconductor. Generally speaking, lower PL signals suggest higher photoinduced electron–hole pair separation efficiency. Fig. 7a presents the PL spectra of the prepared samples with the excitation wavelength of 360 nm. Pure $BiVO_4$ displays the highest PL intensity. In contrast, the $BiVO_4/Ag/Cu_2O$ nanocomposite possesses the lowest PL signal. The shift of the PL peaks further demonstrated the interaction among Cu_2O, Ag and $BiVO_4$. The result indicated that the recombination rate of photoinduced electron–hole pairs was efficiently inhibited through the modification of Cu_2O and Ag on the surface of $BiVO_4$ nanoparticles.

To more deeply study the photogenerated electron migration properties and the photoresponse ability of the prepared samples, some photoelectrochemical characteristics of the prepared samples have been measured. It is well known that the photocurrent response measurement is an efficient method to study the electron transfer dynamics and the photogenerated charge separation ability among the prepared composites. Fig. 7b displays the photocurrent response results based on the pure $BiVO_4$, $BiVO_4/Cu_2O$, $BiVO_4/Ag$ and $BiVO_4/Ag/Cu_2O$ samples. Under visible light irradiation, all the samples present a fast increased photocurrent response that remains constant at a relatively high value. By contrast, in the dark, the photocurrent response intensity stays at a low value. In addition, the prepared $BiVO_4/Ag/Cu_2O$ nanocomposite presents the highest photocurrent response density compared with those of the other three samples. The higher photocurrent response density implies that the prepared $BiVO_4/Ag/Cu_2O$ nanocomposite possesses excellent photogenerated charge separation efficiency compared to the pristine $BiVO_4$, binary $BiVO_4/Cu_2O$ and $BiVO_4/Ag$ composites. EIS measurement is another characterization that shows the photogenerated charge migration process of the prepared samples at solid/electrolyte interfaces. The smaller the arc radius is, the higher the transportation efficiency of the samples. The corresponding EIS measurements of the samples are shown in Fig. 7c. It is clear that the diameter of the arc radius is in the order $BiVO_4 > BiVO_4/Cu_2O > BiVO_4/Ag > BiVO_4/Ag/Cu_2O$, which indicates that the prepared $BiVO_4/Ag/Cu_2O$ nanocomposite presents a more efficient photogenerated charge separation and faster interfacial charge migration ability. Additionally, the polarization curves of as-prepared samples were also measured to investigate the photocurrent response with the changes in applied potential. This measurement was conducted in the applied potential region of −0.3 V to −1.2 V, and the results are disclosed in Fig. 7d. It can be seen that the prepared $BiVO_4/Ag/Cu_2O$ nanocomposite presents a much higher cathodic photocurrent density than the other three samples, which means enhanced photocatalytic performance and degradation ability, consistent with the following photocatalytic degradation performance for TC removal. The results mentioned above demonstrate the excellent photoelectrochemical properties and charge separation efficiency of the prepared $BiVO_4/Ag/Cu_2O$ nanocomposite, and the enhanced photocatalytic activity can be referred to the fast photogenerated electron–hole transfer and improved response ability to visible light brought about by the co-modification with the metallic Ag and Cu_2O

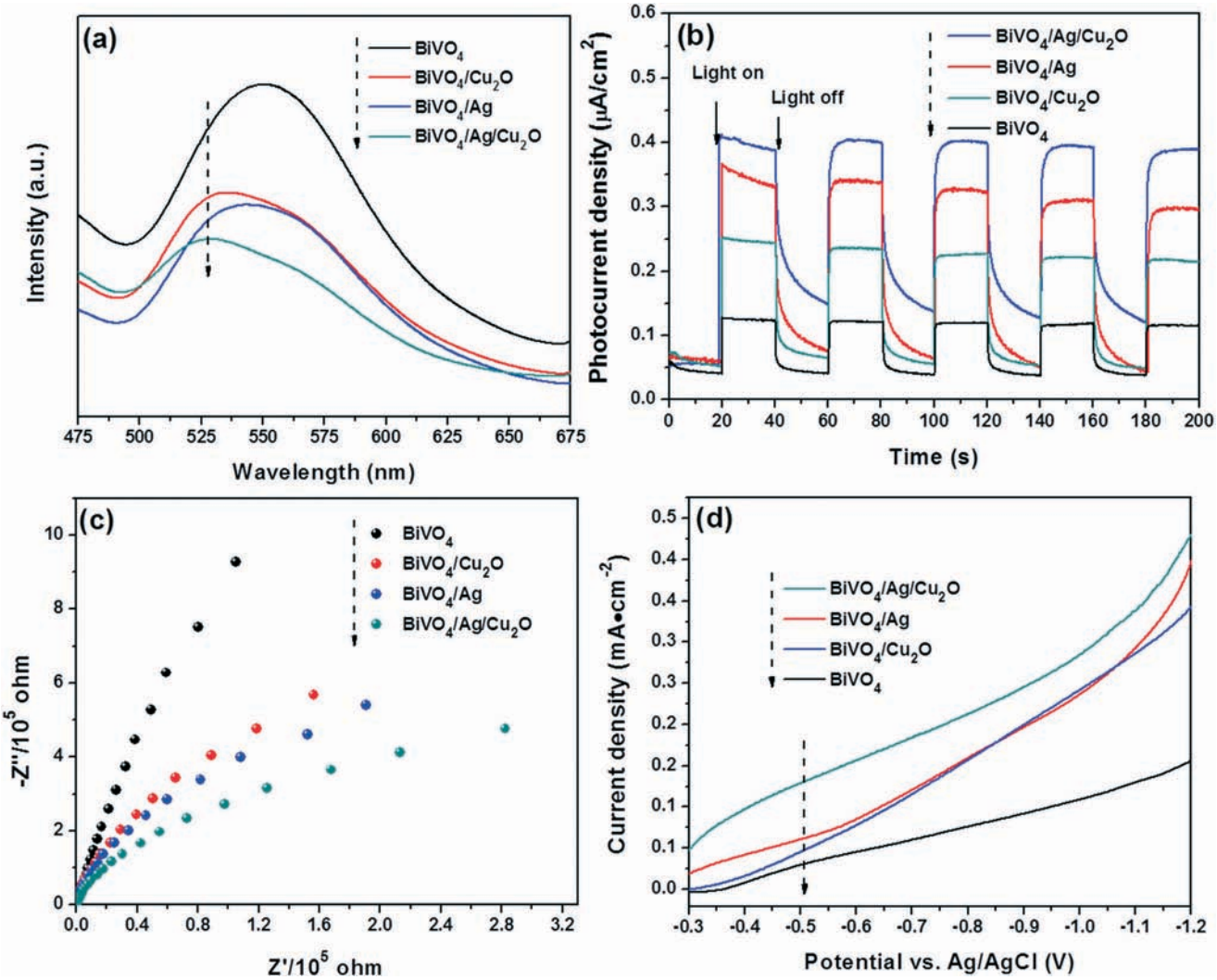

Fig. 7 (a) Photoluminescence spectra, (b) photocurrent response density, (c) EIS Nyquist plots and (d) the cyclic voltammograms of $BiVO_4$, $BiVO_4$/Cu_2O, $BiVO_4$/Ag and $BiVO_4$/Ag/Cu_2O.

nanoparticles on the surface of $BiVO_4$ to synthesize the $BiVO_4$/Ag/Cu_2O nanocomposite.

3.5. Photocatalytic degradation of TC

To evaluate the photocatalytic capability of the prepared $BiVO_4$/Ag/Cu_2O nanocomposites, a typical antibiotic, tetracycline, was chosen as the target contaminant. Meanwhile, considering practical application, various reaction conditions such as different coating contents of Cu_2O and Ag nanoparticles, initial TC concentration, supporting electrolytes and different irradiation conditions were also studied.

3.5.1. The influence of Cu_2O and Ag content. Fig. 8 shows the photocatalytic activities of the as-prepared $BiVO_4$, Cu_2O and $BiVO_4$/Ag/Cu_2O nanocomposites with different mass ratios for the photocatalytic degradation of TC under visible light irradiation. The photocatalytic degradation performance of the above photocatalysts was evaluated *via* the variations of the TC concentration ratios (C/C_0, with C_0 and C standing for the initial and residual concentrations of the TC solutions, respectively). Fig. 8a presents the results of the TC degradation based on the as-prepared $BiVO_4$/Cu_2O with different mass ratios of Cu_2O nanoparticles on the surface of $BiVO_4$. The photolysis results of TC degradation under visible light irradiation indicate that the self-degradation of TC is negligible under the lamp irradiation. After irradiation for 60 min, the concentration of TC obviously decreased in the presence of the photocatalyst. In Fig. 8a, we can see that when pure $BiVO_4$ was added into this photocatalytic system, just 42.9% of TC was degraded. Once the Cu_2O nanoparticles were coated on the surface of $BiVO_4$ to synthesise the hybrid $BiVO_4$/Cu_2O, the photocatalytic degradation efficiency of TC increased, and the photocatalytic degradation rate increased with the increased mass ratio of Cu_2O nanoparticles. When the mass ratio of Cu_2O on $BiVO_4$ reached 3%, 65.17% TC degradation efficiency can be obtained within 60 min of irradiation. This can be explained by the following two reasons. On the one hand, the coating of Cu_2O on the surface of $BiVO_4$ can result in better harvest of incident light; on the

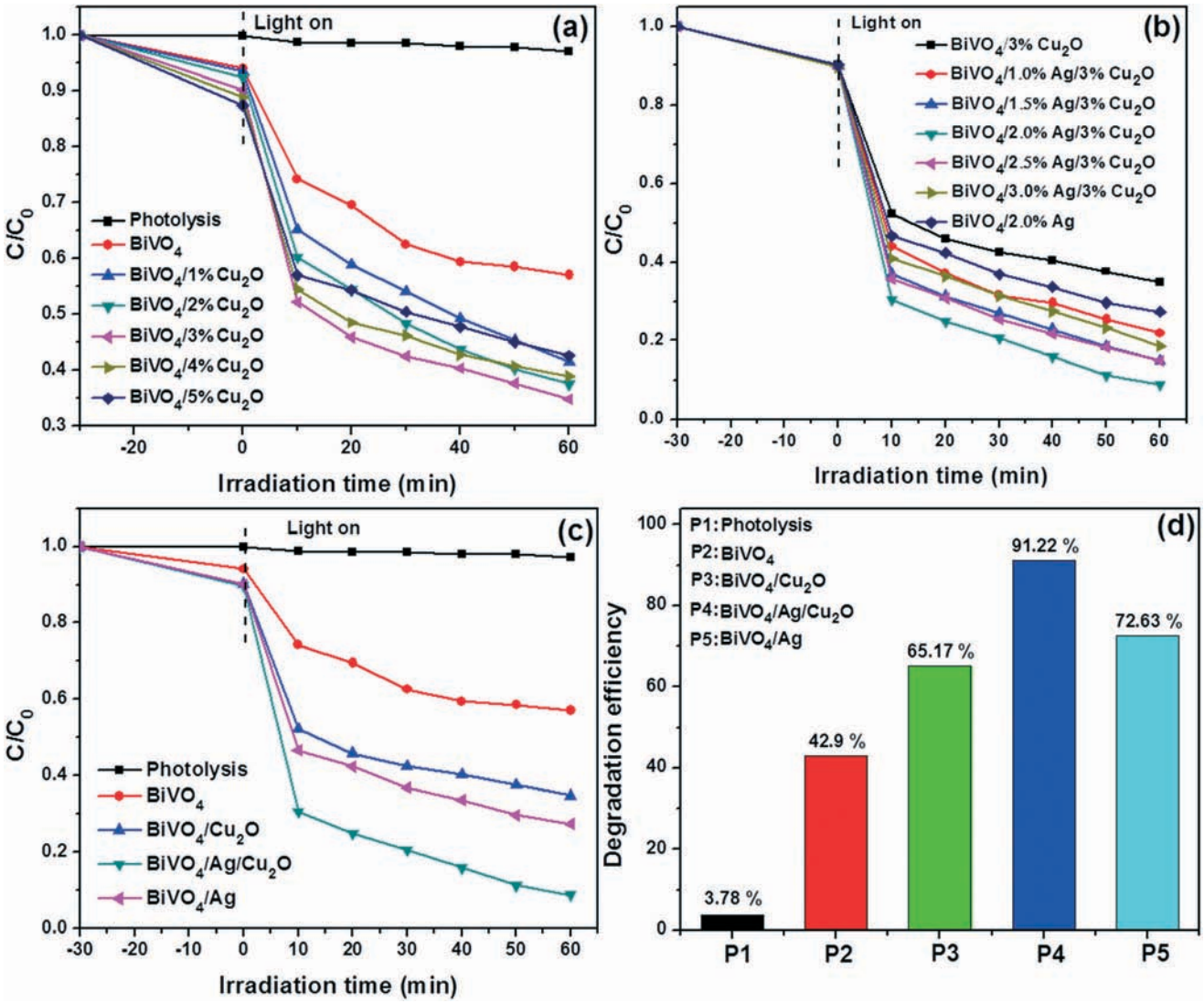

Fig. 8 Photocatalytic degradation of TC based on (a) binary $BiVO_4/Cu_2O$ composites with different mass ratios of Cu_2O and (b) ternary $BiVO_4/Ag/Cu_2O$ nanocomposites with different Ag mass ratios under visible light irradiation. (c and d) Summary of the photocatalytic degradation of TC based on different photocatalysts and corresponding photocatalytic degradation efficiencies.

other hand, due to the existence of Cu_2O particles, heterojunctions between Cu_2O and $BiVO_4$ were introduced, which can promote the separation of photogenerated electrons and holes as well as accelerate the diffusion of charge carriers to the surface of the photocatalyst. But when the amount of Cu_2O further increased, the photocatalytic activity decreased. This could be due to the excessive amount of Cu_2O that acts as a kind of recombination center rather than an electron pathway and promotes the recombination of electrons and holes in $BiVO_4$. Hence we take the optimal Cu_2O loading on $BiVO_4$ to be 3%.

To further improve the performance of the $BiVO_4/Cu_2O$ photocatalysts, metallic Ag was added to the optimum $BiVO_4$/3%Cu_2O photocatalysts to form the ternary $BiVO_4/Ag/Cu_2O$ nanocomposite. In Fig. 8b, it is clearly seen that when the mass ratio of metallic Ag coated on the optimum 3% Cu_2O increases to 2%, the photocatalytic degradation efficiency further increases. Further increasing the amount of Ag can make the degradation efficiency decrease, which means that at the appropriate amount Ag can serve as an electron bridge and pathway to accelerate the electron transfer efficiency. However, excess metallic Ag will become the recombination center, resulting in decreased photocatalytic performance. The results mean that both Cu_2O and Ag contents played critical roles for the eventual photocatalytic degradation performance. The optimum mass ratios of Cu_2O and Ag for the photocatalytic degradation of TC appeared to be *ca.* 3% and 2%, respectively. Further increases of Cu_2O and Ag contents on the surface of $BiVO_4$ even result in a decrease in the degradation efficiency for the degradation of TC. This phenomenon implied that at the optimum coating amount, Cu_2O and Ag nanoparticles can be finely dispersed and well-distributed on the $BiVO_4$ surface and lead to enhanced photocatalytic activity. However, at high content of the coating nanoparticles,

the coated nanoparticles prefer to agglomerate into large bulk particles and lead to the decrease of the photocatalytic efficiency. Furthermore, the presence of an excessive number of Cu_2O and Ag nanoparticles will reduce the exposed area directly under the incoming light and can create electron–hole recombination centers and reduce the efficiency of charge separation.

To more clearly evaluate the performance of the different photocatalysts and make comparisons, Fig. 8c and d summarize the optimum photocatalytic performance of $BiVO_4$, $BiVO_4/Cu_2O$, $BiVO_4/Ag$ and $BiVO_4/Ag/Cu_2O$ photocatalysts. We can see that the $BiVO_4/Ag/Cu_2O$ composite presents the highest TC degradation efficiency in the optimum condition and reaches 91.22% within 60 min. The degradation rate of TC over the catalysts can be arranged in the order $BiVO_4/Ag/Cu_2O > BiVO_4/Ag > BiVO_4/Cu_2O > BiVO_4$. As compared with pure $BiVO_4$, both $BiVO_4/Ag$ and $BiVO_4/Cu_2O$ exhibit enhanced photocatalytic TC degradation efficiency, demonstrating that Ag and Cu_2O can be used as co-catalysts to enhance the photocatalytic TC degradation activity. Importantly, the highest TC degradation rate is achieved for the sample $BiVO_4/Ag/Cu_2O$ owing to the synergetic effect of Ag and Cu_2O on the photocatalytic activity of $BiVO_4$.

3.5.2. The influence of initial TC concentration. To study the effect of initial TC concentration on the degradation rate, five initial concentrations of 20, 30, 40, 50 and 60 mg L^{-1} were investigated. Fig. 9a presents the results of TC degradation as a function of irradiation time at different initial concentrations, from which we can see that the removal efficiency of TC decreases from 91.22% to 46.42% when the initial concentration of TC increases from 20 mg L^{-1} to 60 mg L^{-1}. It is well-known that light penetration through the aqueous solution is influenced by the initial TC concentration.[47] The increase of the initial TC concentration will

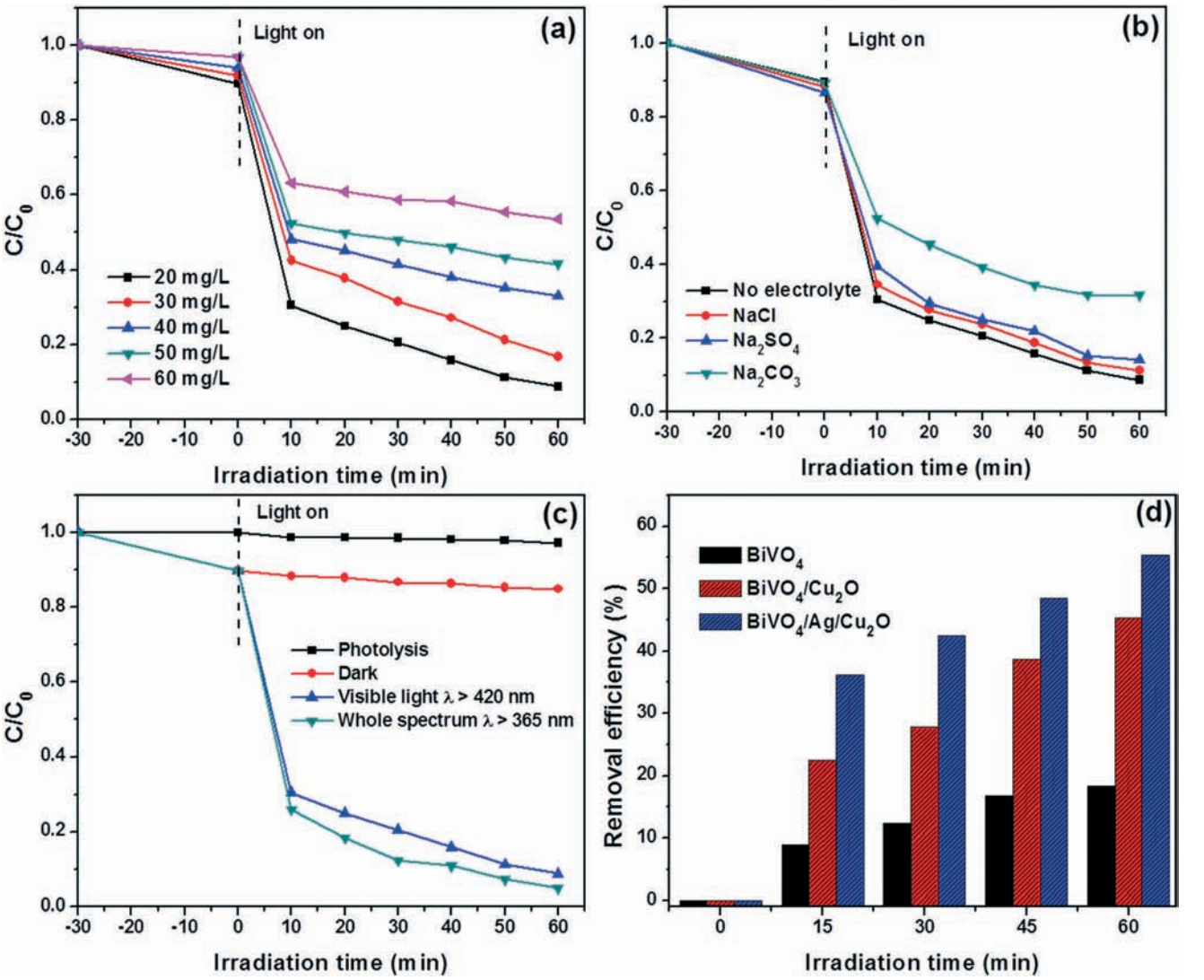

Fig. 9 The influence of (a) initial TC concentration, (b) supporting electrolytes and (c) different light irradiation conditions on $BiVO_4/Ag/Cu_2O$ composites. (d) Total organic carbon (TOC) removal efficiencies of the prepared $BiVO_4$, $BiVO_4/Cu_2O$ and $BiVO_4/Ag/Cu_2O$ composites under visible light irradiation.

reduce the degree of light penetration and lead to fewer photons arriving at the surface of the photocatalysts. In addition, during the photocatalytic degradation process, the increasingly formed intermediates at high initial TC concentration compete with the TC molecules for the limited adsorption and catalytic activity sites on the $BiVO_4/Ag/Cu_2O$ surface, which will inhibit the degradation of TC molecules. Therefore, to reduce the negative effect of the initial TC concentration and to obtain a full understanding of the photocatalytic activity of the prepared samples, an initial TC concentration of 20 mg L^{-1} was chosen throughout the experiments.

3.5.3. The influence of supporting electrolyte. In real applications, many co-existing substances will unavoidably affect the photocatalytic removal efficiency of the target contaminant. Electrolytes, especially for some hydroxyl radical scavengers, can greatly affect the photocatalytic performance of the photocatalyst in the degradation of pollutants in aqueous solutions. Herein, we studied the effect of chloride, sulfate and bicarbonate ions as the most common co-existing anions in natural water on the photocatalytic removal of TC by $BiVO_4/Ag/Cu_2O$ nanocomposites. Fig. 9b shows the results of TC degradation in the presence of these electrolytes at a concentration of 0.05 mol L^{-1}. It can be seen that chloride shows minimal impact on the photocatalytic degradation efficiency of the photocatalysts, and bicarbonate presents the largest effect among the three supporting electrolytes. Although sulfate presents a more negative effect on TC degradation than chloride, the difference can almost be ignored. The reason for the inhibition effect of the sulfate ions on the photocatalytic degradation of TC is mainly competitive adsorption of the reaction sites between SO_4^{2-} and TC molecules on the surface of the photocatalyst.[47] It is known that the initial unadjusted pH of the TC solution is nearly neutral. Under neutral conditions, both carbonate and bicarbonate ions exist. The largest effect of Na_2CO_3 on TC photocatalytic degradation can be attributed to the existence of carbonate and bicarbonate ions. It has been reported that carbonate and bicarbonate can serve as radical scavengers,[48] which can consume the hydroxyl radicals produced at the surface of the $BiVO_4/Ag/Cu_2O$ photocatalysts. This consumption process will result in the decrease of the reactive radicals that react with the TC molecules, and the photocatalytic removal efficiency of TC will be inhibited to a great extent.

3.5.4. The influence of light irradiation condition. The maximum employment of the sun's energy is one of the hot spots in the photocatalytic field, which can bring about both the reduction of fossil energy consumption and the remediation of the environment. Thus, to investigate the photocatalytic performance of the prepared photocatalysts in the whole spectrum, control experiments were conducted for the photocatalytic degradation of TC using a Xe lamp with or without an optical filter. When the $BiVO_4/Ag/Cu_2O$ was irradiated with the Xe lamp without the optical filter, the performance of the photocatalysts under the full spectrum can be obtained. The result of TC removal under different irradiation conditions by the $BiVO_4/Ag/Cu_2O$ photocatalysts is presented in Fig. 9c. It is clearly seen that when the prepared $BiVO_4/Ag/Cu_2O$ nanocomposites was under full spectrum illumination ($\lambda >$ 365 nm), nearly all of the TC was removed from the solution in 60 min. When the $BiVO_4/Ag/Cu_2O$ photocatalysts were exposed to visible light ($\lambda >$ 420 nm), after 60 min 91.22% of the TC was removed. Meanwhile, it should be noted that the percent photolysis of TC degradation under illumination without the presence of photocatalysts was less than 5%. In the photocatalytic reaction system, due to the existence of a band gap, the photocatalysts can be excited only by the photons which own energy higher than that of the band gap to generate electrons and holes. Besides, the shorter the wavelength of the light, the greater the energy its photons possess.[47] Therefore, in the absence of the optical filter, the photocatalysts can utilize the full spectrum of the Xe lamp, resulting in increased photocatalytic degradation performance. Quite evidently, the removal of TC under dark conditions was attributed to the adsorption process.

3.6. Mineralization ability and 3D EEMs analysis

The mineralization ability was also a very important factor for evaluating the performance of the photocatalysts. Hence the total organic carbon (TOC) removal efficiency has been investigated in this study. As shown in Fig. 9d, after 60 min of visible light irradiation, the mineralization rates for the pure $BiVO_4$, $BiVO_4/Cu_2O$ and $BiVO_4/Ag/Cu_2O$ were 18.36%, 42.27% and 55.32%, respectively. The highest TOC removal efficiency means that the prepared $BiVO_4/Ag/Cu_2O$ photocatalysts presented not only improved TC photocatalytic degradation rate but also enhanced mineralization ability.

Moreover, 3D EEMs technology was used to deeply understand the TC degradation process based on $BiVO_4/Ag/Cu_2O$ photocatalysts, which includes adsorption and photodegradation processes. Six samples were collected under different conditions and the results are shown in Fig. 10. According to previous studies, during the degradation process of TC, two main peaks would appear, peak A at $\lambda_{ex}/\lambda_{em}$ = (305–330 nm)/(430–450 nm) and peak B at $\lambda_{ex}/\lambda_{em}$ = (240–250 nm)/(435–450 nm), referring to the humic acid-like and fulvic acid-like fluorescence regions, respectively. Moreover, it is known that TC molecules have a fluorescence quenching effect.[49,50] Thus, in the EEMs results of the original TC samples or the samples obtained after the dark adsorption process, no obvious fluorescence signal can be observed (Fig. 10a and b), indicating that no TC molecules were degraded or changed into other products during the dark adsorption process. However, when the reaction system was exposed to visible light, two characteristic peaks referring to the production of humic acid-like and fulvic acid-like organic matter appeared, which might be attributed to the degradation of TC molecules by the $BiVO_4/Ag/Cu_2O$ nanocomposite. Furthermore, it should be noted that the EEMs results show that the fluorescence intensity increased with the irradiation time increasing from 10 min to 40 min (Fig. 10c–e), which indicates the accumulation of the humic acid-like and fulvic

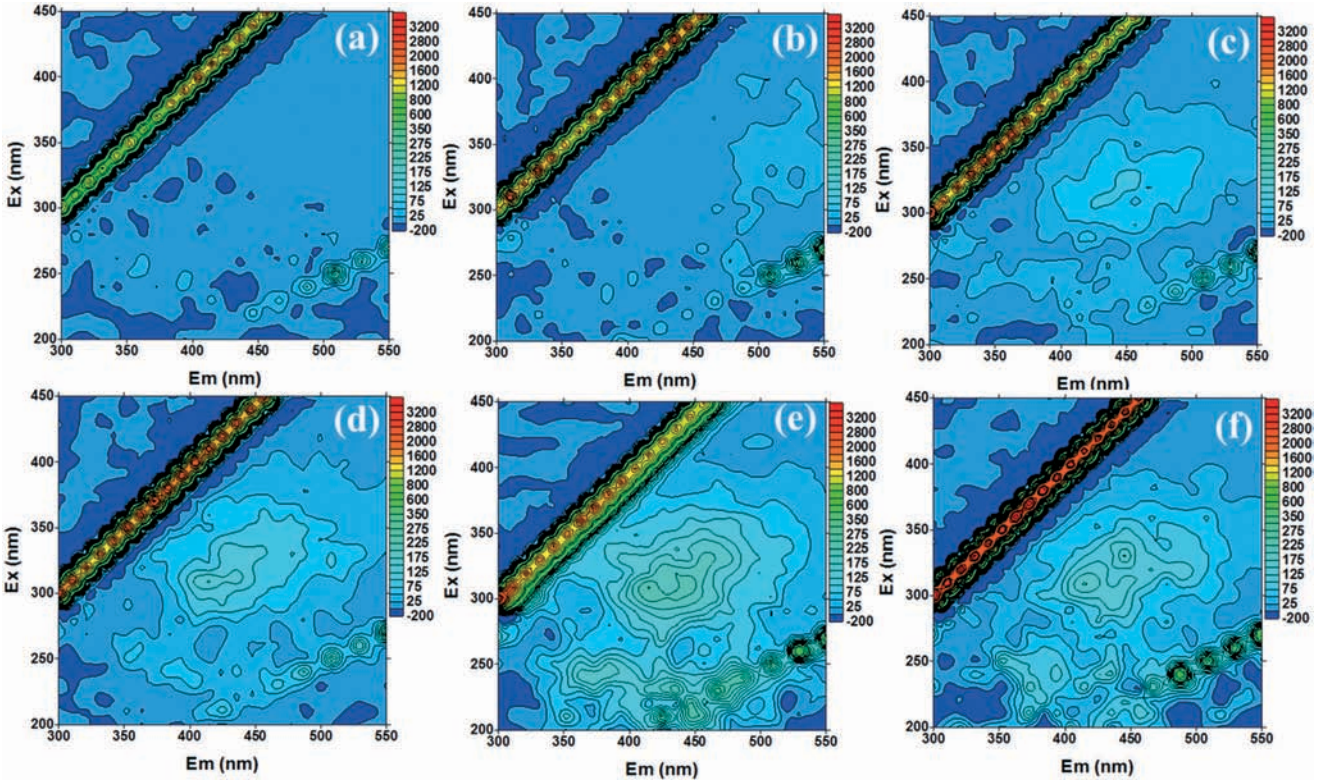

Fig. 10 3D EEMs results of (a) original TC solution, (b) sample obtained from TC solution after 30 min of dark adsorption process, and (c–f) samples obtained with the visible light irradiation time of 10 min, 20 min, 40 min and 60 min, respectively.

acid-like organic matter. But as shown in Fig. 10f, when the irradiation time reaches 60 min, the fluorescence intensity of the characteristic peaks decreases to some extent, indicating the thorough decomposition and partial mineralization of TC molecules into CO_2 and H_2O. This phenomenon also demonstrated the high mineralization ability of the prepared $BiVO_4$/Ag/Cu_2O photocatalyst.

3.7. Photocatalyst recyclability

To study the photocatalytic stability of the prepared $BiVO_4$/Ag/Cu_2O photocatalysts, five repetitive reaction processes for the degradation of TC have been conducted. When the previous reaction process was finished, the photocatalyst was collected, washed thoroughly and dried for the subsequent cycle experiment. As the results disclosed in Fig. 11, even after five repeated experiments, the removal efficiency of TC based on $BiVO_4$/Ag/Cu_2O photocatalyst still remained at 88.12%, which implied the excellent performance and stability of the prepared photocatalysts. To further investigate the change of the prepared $BiVO_4$/Ag/Cu_2O photocatalyst, XPS measurements of the photocatalyst after five repeated experiments were conducted and the relative spectra are provided in Fig. 12. In Fig. 12a and c, compared with the results shown in Fig. 5, we can see that there are no significant changes appearing in the survey XPS spectra and high resolution XPS spectra of Ag 3d of the photocatalyst after the photocatalytic process, which indicates the overall stability of the prepared $BiVO_4$/Ag/Cu_2O samples. As for the high-resolution XPS spectra of Cu 2p (Fig. 12b), we can see that after five repeated photocatalytic experiments, the peaks of Cu_2O at 931.8 eV and 951.7 eV decrease, and the peaks located at 933.9 eV and 954.3 eV that belong to Cu^{2+} increase, which means that during the photocatalytic process, some part of the Cu_2O on the surface would be oxidized into CuO owing to the high density of light irradiation. This phenomenon has also been widely observed by

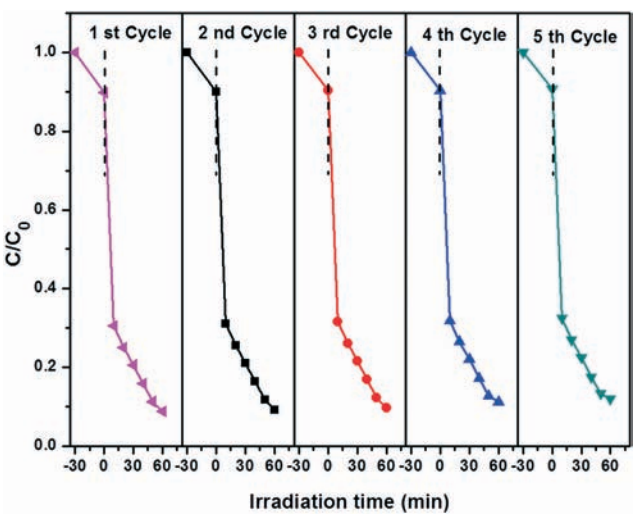

Fig. 11 Recycle experiments of $BiVO_4$/Ag/Cu_2O nanocomposites for the photocatalytic degradation of TC.

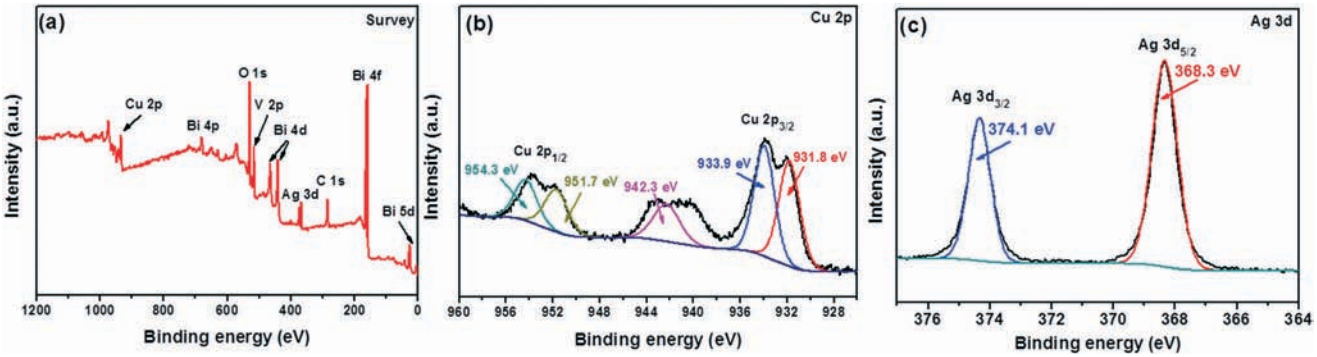

Fig. 12 The survey XPS spectra (a) and high-resolution XPS spectra of Cu 2p (b) and Ag 3d (c) for $BiVO_4/Ag/Cu_2O$ nanocomposites after recycle experiments.

other researchers for the Cu_2O based reaction system.[43,51–53] However, it should be noted that despite the existence of the valence state change of the Cu element, the photocatalytic activity of the prepared $BiVO_4/Ag/Cu_2O$ photocatalyst still kept a relative stability, and the photocatalytic performance was very high even after five repeated experiments. This phenomenon could be attributed to the recrystallization process of the photocatalyst. That is to say, during the photocatalytic process, part of the Cu_2O would be changed into CuO to make this reaction system become more stable, which seems like a self-optimizing process, resulting in this reaction system being more efficient. The recrystallization process of the Cu_2O based reaction system has been fully investigated by Zhang and co-workers.[54] This is the reason for the high photocatalytic performance of the prepared $BiVO_4/Ag/Cu_2O$ in the repeated experiments despite the existence of the change of the Cu element valence state.

3.8. Possible photocatalytic reaction mechanism

To investigate the predominant active species for TC degradation in the photocatalytic reaction process and understand the reaction mechanism in depth, three typical scavengers, isopropanol (IPA), ethylenediaminetetraacetic acid disodium (EDTA-2Na) and 1,4-benzoquinone (BQ) were used for the investigation of the hydroxyl radical ($^{\cdot}OH$), hole (h^+) and superoxide radical ($^{\cdot}O_2^-$), respectively.[19,41] The concentrations of these three added scavengers in the reaction system were 1 mM. Additionally, N_2 purging experiments were also conducted to confirm the role of $^{\cdot}O_2^-$ in the photocatalytic reaction process. As for the experiment conducted under a N_2 atmosphere, before the experiment began, the reaction solution was purged by high purity N_2 (> 99.999%) for 1 hour to remove as much of the dissolved O_2 as possible, and the N_2 purging was continued throughout the photocatalytic process. As depicted in Fig. 13a and b, when EDTA-2Na or BQ was added into this reaction system based on pure $BiVO_4$, the photocatalytic removal efficiency of TC decreased greatly. In particular, with the addition of EDTA-2Na, the photocatalytic degradation process was nearly stopped, which only resulted in 8.17% TC removal efficiency, implying that h^+ served as the major reaction species. Meanwhile, the photocatalytic degradation rate of TC also decreased from 42.91% to 26.56% under the purging of N_2, which indicates that $^{\cdot}O_2^-$ played a vital role in TC degradation in the $BiVO_4$ based reaction system. However, the effect of the addition of 1 mM IPA can nearly be ignored, which means that $^{\cdot}OH$ almost did not take part in this reaction process. As for the system based on $BiVO_4/Ag/Cu_2O$, the reaction process was a little different. As displayed in Fig. 13c and d, just like in the pure $BiVO_4$ reaction system, when EDTA-2Na was added, the TC removal efficiency decreased from 91.22% to 11.23%, suggesting the leading role of h^+ in the reaction process. Meanwhile, with the addition of BQ or the purging of N_2 without any scavenger, the photocatalytic activity of $BiVO_4/Ag/Cu_2O$ was also inhibited greatly, which demonstrates that the dissolved oxygen could act as a photogenerated electron scavenger to produce $^{\cdot}O_2^-$ radical species. Moreover, different from the pure $BiVO_4$ reaction system, the addition of IPA also resulted in the decreased removal efficiency of TC to some extent, which indicates that $^{\cdot}OH$ was also produced and took part in the photocatalytic degradation process. According to the results mentioned above, we can preliminary conclude that in the pure $BiVO_4$ reaction system, h^+ and O_2^- were the main reaction species, while in the $BiVO_4/Ag/Cu_2O$ based reaction system, h^+, $^{\cdot}O_2^-$ and $^{\cdot}OH$ were all produced and participated in the TC degradation process.

To further study and confirm the roles of $^{\cdot}O_2^-$ and $^{\cdot}OH$ in the photocatalytic degradation process of TC by $BiVO_4/Ag/Cu_2O$, DMPO spin-trapping technology was utilized. The results are disclosed in Fig. 14. As shown in Fig. 14a, under dark conditions, no obvious peak could be found for both $BiVO_4$ and $BiVO_4/Ag/Cu_2O$. However, after the catalysts were exposed to visible light for 10 min, the characteristic peaks of the DMPO–$^{\cdot}O_2^-$ adduct appeared for both pure $BiVO_4$ and $BiVO_4/Ag/Cu_2O$ nanocomposite. Therefore, $^{\cdot}O_2^-$ was demonstrated to be produced in the photocatalytic process. Additionally, the peak intensity of the DMPO–$^{\cdot}O_2^-$ adduct referring to the $BiVO_4/Ag/Cu_2O$ nanocomposite was much higher than that of pristine $BiVO_4$, indicating that the generation amount of $^{\cdot}O_2^-$ by $BiVO_4/Ag/Cu_2O$ was more than that of pristine $BiVO_4$. Moreover, the generation of the hydroxyl radical

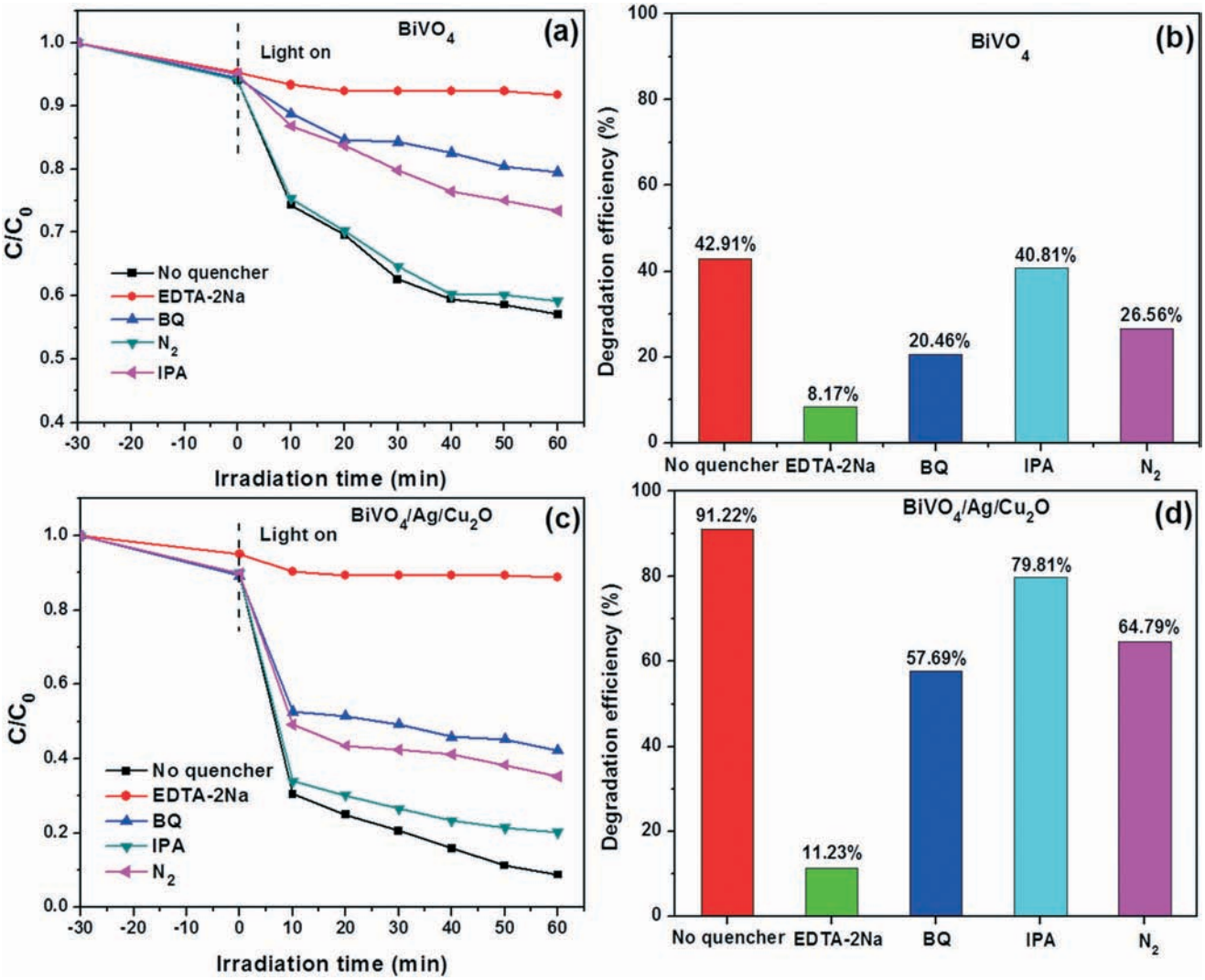

Fig. 13 Trapping experiments for the photocatalytic degradation of TC and the corresponding photocatalytic removal efficiency over pure (a and b) $BiVO_4$ and (c and d) $BiVO_4/Ag/Cu_2O$ composite under visible light irradiation.

among the photocatalytic processes was also detected using the DMPO technology (Fig. 14b). Similarly, no obvious signal could be observed under dark conditions for both pristine $BiVO_4$ and $BiVO_4/Ag/Cu_2O$ composite. Under visible light irradiation for 10 min, obvious signals of $^{\cdot}OH$ were observed for $BiVO_4/Ag/Cu_2O$ composite in the measurement, while under the same conditions, the signals of $^{\cdot}OH$ for pristine $BiVO_4$ could nearly be ignored. This result implied that $^{\cdot}OH$ was produced in the $BiVO_4/Ag/Cu_2O$ based reaction system and took part in the photocatalytic reaction process, while nearly no $^{\cdot}OH$ can be detected in the pristine $BiVO_4$ system. All in all, for the $BiVO_4/Ag/Cu_2O$ nanocomposite, h^+ and $^{\cdot}O_2^-$ species played major roles in TC degradation in the photocatalytic reaction system; meanwhile the $^{\cdot}OH$ species also participated in the photocatalytic reaction process, contributing to the enhanced performance to some extent.

It was reported that the separation rate of photogenerated electrons and holes plays a vital role in the photocatalytic degradation of pollutants.[32,55] According to previous reports, the potential of $OH^-/^{\cdot}OH$ couples is about 2.4 eV, located between the VB of Cu_2O and that of $BiVO_4$.[19,56] The VBs of $BiVO_4$ and Cu_2O are +2.76 eV and +0.6 eV, respectively. The CB of $BiVO_4$ and Cu_2O are located at +0.3 eV and −1.4 eV, respectively.[32,57] That is to say, the holes on the VB of $BiVO_4$ have the ability to react with OH^- to generate $^{\cdot}OH$, while the holes on the VB of Cu_2O cannot do that. Therefore, according to the results of the trapping experiments and the ESR measurement, we assume that the typical p–n heterojunction charge transfer was more coincidental for the $BiVO_4/Cu_2O$ nanocomposites (Scheme 1a). Under visible light irradiation, both $BiVO_4$ and Cu_2O can exist, and then the photogenerated holes on the VB of $BiVO_4$ will be transported to that of Cu_2O; meanwhile, the photogenerated electrons on the CB of Cu_2O will transfer to that of $BiVO_4$. Therefore, the density of holes in the VB of $BiVO_4$ decreases while that in the VB of Cu_2O increases. Owing to the less positive position of the VB of Cu_2O, the holes on Cu_2O do not have enough energy to oxidize OH^- or H_2O to generate $^{\cdot}OH$. Thus the prepared $BiVO_4/$

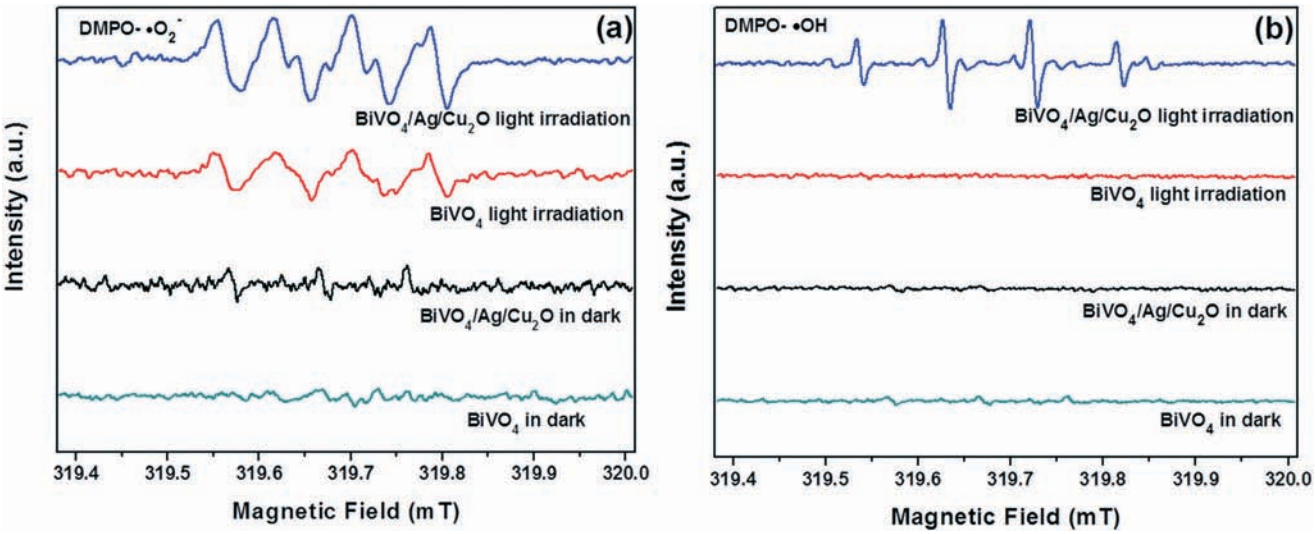

Fig. 14 ESR spectra of radical adducts trapped by DMPO ($^{\cdot}O_2^-$ and $^{\cdot}OH$) for (a) $BiVO_4$ and (b) $BiVO_4/Ag/Cu_2O$ nanocomposite based reaction systems in the dark and under visible light irradiation.

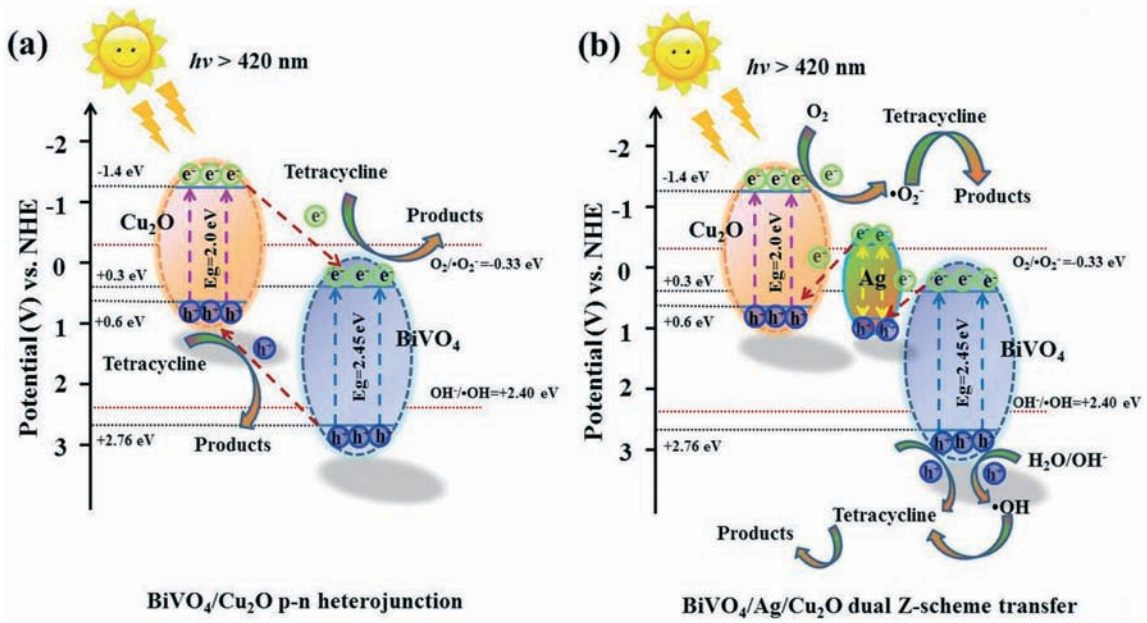

Scheme 1 Schematic illustration of the proposed reaction mechanism in the (a) $BiVO_4/Cu_2O$ and (b) $BiVO_4/Ag/Cu_2O$ nanocomposite based reaction systems towards TC degradation under visible light irradiation.

Cu_2O generates very little $^{\cdot}OH$. On the contrary, the ESR measurement means that the photogenerated holes of the sample $BiVO_4/Ag/Cu_2O$ accumulate in the VB of $BiVO_4$, indicating a different charge transfer mechanism.

Combining the discussion and the experimental results presented above, a dual Z-scheme photocatalytic mechanism of the prepared $BiVO_4/Ag/Cu_2O$ is proposed and illustrated in Scheme 1b. In the photocatalytic reaction system, before the light irradiation starts, the Fermi levels have reached equilibrium at the interface of $BiVO_4$, Ag and Cu_2O. Then under visible light irradiation, both $BiVO_4$ and Cu_2O can be photoexcited to produce photogenerated electrons and holes. In addition, the photogenerated electrons produced on the CB of $BiVO_4$ will transport to metallic Ag. Simultaneously, due to the strong SPR effect of Ag nanoparticles, an enhanced local electric field will emerge on the interface of Ag nanoparticles, which can make the photogenerated electrons of Ag migrate to the VB of Cu_2O and recombine with the holes *via* plasmon-induced resonance energy transfer or direct electron migration. Subsequently, the photogenerated electrons that remained and accumulated in the CB of Cu_2O have enough energy to react with dissolved O_2 to produce $^{\cdot}O_2^-$, and the accumulated holes on the VB of $BiVO_4$ with high energy can degrade TC molecules directly or react with H_2O or OH^- to

generate $^{\cdot}OH$ to degrade TC. It should be noted that this type of electron–hole migration pathway not only can accelerate the transfer rate of charges and reduce the recombination efficiency but also can retain the strong redox ability by retaining the photogenerated electrons on the more negative CB of Cu_2O and holes on the more positive VB of $BiVO_4$. Because this transfer process is similar to that of the Z-scheme mechanism, just divided into a double "Z" shape, the "dual Z-scheme charge transfer" mechanism is more suitable and accurate to describe the mechanism that occurs in this photocatalytic reaction system.

4. Conclusion

To sum up, in this study we successfully constructed a plasmon resonance excited dual Z-scheme $BiVO_4$/Ag/Cu_2O nanocomposite based on $BiVO_4$ nanoparticles by a facile impregnation route combined with a photodeposition strategy. Owing to the synergetic effect of metallic Ag and Cu_2O nanoparticles, the prepared $BiVO_4$/Ag/Cu_2O nanocomposite presented an enhanced photocatalytic performance towards TC removal, showing 91.22% removal efficiency under visible light irradiation within 60 min. Control experiments showed that the optimal initial TC concentration was 10 mg L^{-1}, and bicarbonate ions presented a great inhibition effect on TC degradation. In broad spectrum light irradiation, enhanced photocatalytic performance was obtained. In addition, the prepared $BiVO_4$/Ag/Cu_2O nanocomposite also showed enhanced mineralization ability, as 55.32% TOC removal efficiency could be obtained under visible light irradiation for 60 min. The excellent photocatalytic degradation performance and mineralization ability of TC based on the $BiVO_4$/Ag/Cu_2O photocatalysts can be explained by the following two reasons. On the one hand, the introduction of Cu_2O and Ag on the surface of $BiVO_4$ can result in improved visible-light absorption ability; on the other hand, due to the enhanced SPR effect caused by metallic Ag, a local electric field will be established, which leads to a dual Z-scheme charge transfer pathway in the composite. It not only brings about the fast separation rate of the photogenerated electrons and holes but also retains the strong redox ability of these photogenerated charges. This work provides a new insight into the understanding of the photocatalysis mechanism based on the SPR effect of Ag, and promotes the potential of visible light excited photocatalysts for real wastewater remediation.

Acknowledgements

The study was financially supported by Projects 51579096, 51521006, 51222805, 51508175 and 51409024 supported by the National Natural Science Foundation of China, the National Program for Support of Top-Notch Young Professionals of China (2012), the Program for New Century Excellent Talents in University from the Ministry of Education of China (NCET-11-0129), and the Hunan Province Innovation Foundation for Postgraduate (CX2015B095).

References

1 M. Yan, Y. Hua, F. Zhu, W. Gu, J. Jiang, H. Shen and W. Shi, *Appl. Catal., B*, 2017, **202**, 518–527.
2 S. Leong, D. Li, K. Hapgood, X. Zhang and H. Wang, *Appl. Catal., B*, 2016, **198**, 224–233.
3 J. Jeong, W. Song, W. J. Cooper, J. Jung and J. Greaves, *Chemosphere*, 2010, **78**, 533–540.
4 S. Kim, P. Eichhorn, J. N. Jensen, A. S. Weber and D. S. Aga, *Environ. Sci. Technol.*, 2005, **39**, 5816–5823.
5 Y. Zhang, G. M. Zeng, L. Tang, D. L. Huang, X. Y. Jiang and Y. N. Chen, *Biosens. Bioelectron.*, 2007, **22**, 2121–2126.
6 M. Cao, P. Wang, Y. Ao, C. Wang, J. Hou and J. Qian, *J. Colloid Interface Sci.*, 2016, **467**, 129–139.
7 Y. Wang, H. Zhang, J. Zhang, C. Lu, Q. Huang, J. Wu and F. Liu, *J. Hazard. Mater.*, 2011, **192**, 35–43.
8 L. Tang, G. M. Zeng, G. L. Shen, Y. P. Li, Y. Zhang and D. L. Huang, *Environ. Sci. Technol.*, 2008, **42**, 1207–1212.
9 J. Xiong, Z. Li, J. Chen, S. Zhang, L. Wang and S. Dou, *ACS Appl. Mater. Interfaces*, 2014, **6**, 15716–15725.
10 Y. Kanigaridou, A. Petala, Z. Frontistis, M. Antonopoulou, M. Solakidou, I. Konstantinou, Y. Deligiannakis, D. Mantzavinos and D. I. Kondarides, *Chem. Eng. J.*, 2017, **318**, 39–49.
11 X. Fu, M. Xie, P. Luan and L. Jing, *ACS Appl. Mater. Interfaces*, 2014, **6**, 18550–18557.
12 L. Jing, Y. Xu, S. Huang, M. Xie, M. He, H. Xu, H. Li and Q. Zhang, *Appl. Catal., B*, 2016, **199**, 11–22.
13 H. Ji, L. Lyu, L. Zhang, X. An and C. Hu, *Appl. Catal., B*, 2016, **199**, 230–240.
14 Y. C. Deng, L. Tang, G. M. Zeng, H. R. Dong, M. Yan, J. J. Wang, W. Hu, J. J. Wang, Y. Y. Zhou and J. Tang, *Appl. Surf. Sci.*, 2016, **387**, 882–893.
15 M. Zhang, W. Luo, Z. Wei, W. Jiang, D. Liu and Y. Zhu, *Appl. Catal., B*, 2016, **194**, 105–110.
16 H. Wang, X. Yuan, Y. Wu, G. Zeng, X. Chen, L. Leng and H. Li, *Appl. Catal., B*, 2015, **174–175**, 445–454.
17 H. Wang, X. Yuan, Y. Wu, G. Zeng, X. Chen, L. Leng, Z. Wu, L. Jiang and H. Li, *J. Hazard. Mater.*, 2015, **286**, 187–194.
18 H. Wang, X. Yuan, G. Zeng, Y. Wu, Y. Liu, Q. Jiang and S. Gu, *Adv. Colloid Interface Sci.*, 2015, **221**, 41–59.
19 Y. C. Deng, L. Tang, G. M. Zeng, J. J. Wang, Y. Y. Zhou, J. J. Wang, J. Tang, Y. N. Liu, B. Peng and F. Chen, *J. Mol. Catal. A: Chem.*, 2016, **421**, 209–221.
20 Y. C. Deng, L. Tang, G. M. Zeng, Z. J. Zhu, M. Yan, Y. Y. Zhou, J. J. Wang, Y. N. Liu and J. J. Wang, *Appl. Catal., B*, 2017, **203**, 343–354.
21 R. Li, F. Zhang, D. Wang, J. Yang, M. Li, J. Zhu, X. Zhou, H. Han and C. Li, *Nat. Commun.*, 2013, **4**, 1432.
22 F. Lin, D. Wang, Z. Jiang, Y. Ma, J. Li, R. Li and C. Li, *Energy Environ. Sci.*, 2012, **5**, 6400–6406.
23 J. Zhang, H. Ma and Z. Liu, *Appl. Catal., B*, 2017, **201**, 84–91.
24 Y. Zhu, Y. Wang, Q. Ling and Y. Zhu, *Appl. Catal., B*, 2017, **200**, 222–229.
25 L. Tang, J. J. Wang, G. M. Zeng, Y. N. Liu, Y. C. Deng, Y. Y. Zhou, J. Tang, J. J. Wang and Z. Guo, *J. Hazard. Mater.*, 2015, **306**, 295–304.

26 H. Wang, X. Yuan, Y. Wu, G. Zeng, W. Tu, C. Sheng, Y. Deng, F. Chen and J. W. Chew, *Appl. Catal., B*, 2017, **209**, 543–553.

27 R. Li, H. Han, F. Zhang, D. Wang and C. Li, *Energy Environ. Sci.*, 2014, **7**, 1369.

28 Z. Y. Bian, Y. Q. Zhu, J. X. Zhang, A. Z. Ding and H. Wang, *Chemosphere*, 2014, **117**, 527–531.

29 W. Wang, X. Huang, S. Wu, Y. Zhou, L. Wang, H. Shi, Y. Liang and B. Zou, *Appl. Catal., B*, 2013, **134–135**, 293–301.

30 P. Zhou, J. Yu and M. Jaroniec, *Adv. Mater.*, 2014, **26**, 4920–4935.

31 X. Wang, G. Liu, Z. G. Chen, F. Li, L. Wang, G. Q. Lu and H. M. Cheng, *Chem. Commun.*, 2009, 3452–3454, DOI: 10.1039/b904668b.

32 J. Fu, S. Cao and J. Yu, *J. Materiomics*, 2015, **1**, 124–133.

33 D. Xu, B. Cheng, S. Cao and J. Yu, *Appl. Catal., B*, 2015, **164**, 380–388.

34 J. C. Wang, L. Zhang, W. X. Fang, J. Ren, Y. Y. Li, H. C. Yao, J. S. Wang and Z. J. Li, *ACS Appl. Mater. Interfaces*, 2015, **7**, 8631–8639.

35 L. J. Zhang, S. Li, B. K. Liu, D. J. Wang and T. F. Xie, *ACS Catal.*, 2014, **4**, 3724–3729.

36 Z. Zhao, W. Zhang, X. Lv, Y. Sun, F. Dong and Y. Zhang, *Environ. Sci.: Nano*, 2016, **3**, 1306–1317.

37 J. J. Wang, L. Tang, G. M. Zeng, Y. N. Liu, Y. Y. Zhou, Y. C. Deng, J. J. Wang and B. Peng, *ACS Sustainable Chem. Eng.*, 2017, **5**, 1062–1072.

38 F. Chen, Q. Yang, X. Li, G. Zeng, D. Wang, C. Niu, J. Zhao, H. An, T. Xie and Y. Deng, *Appl. Catal., B*, 2017, **200**, 330–342.

39 F. Chen, Q. Yang, Y. Zhong, H. An, J. Zhao, T. Xie, Q. Xu, X. Li, D. Wang and G. Zeng, *Water Res.*, 2016, **101**, 555–563.

40 Y. Bu, Z. Chen and C. Sun, *Appl. Catal., B*, 2015, **179**, 363–371.

41 Z. Zhu, Z. Lu, D. Wang, X. Tang, Y. Yan, W. Shi, Y. Wang, N. Gao, X. Yao and H. Dong, *Appl. Catal., B*, 2016, **182**, 115–122.

42 Q. Yuan, L. Chen, M. Xiong, J. He, S.-L. Luo, C.-T. Au and S.-F. Yin, *Chem. Eng. J.*, 2014, **255**, 394–402.

43 W. Wang, J. Wang, Z. Wang, X. Wei, L. Liu, Q. Ren, W. Gao, Y. Liang and H. Shi, *Dalton Trans.*, 2014, **43**, 6735–6743.

44 A. Y. Booshehri, S. Chun-Kiat Goh, J. Hong, R. Jiang and R. Xu, *J. Mater. Chem. A*, 2014, **2**, 6209.

45 M. Ou, Q. Zhong, S. Zhang, H. Nie, Z. Lv and W. Cai, *Appl. Catal., B*, 2016, **193**, 160–169.

46 M. Yan, Y. Wu, Y. Yan, X. Yan, F. Zhu, Y. Hua and W. Shi, *ACS Sustainable Chem. Eng.*, 2016, **4**, 757–766.

47 B. Zhou, X. Zhao, H. Liu, J. Qu and C. P. Huang, *Appl. Catal., B*, 2010, **99**, 214–221.

48 H. Xiao, R. Liu, X. Zhao and J. Qu, *J. Mol. Catal. A: Chem.*, 2008, **286**, 149–155.

49 H. Wang, X. Yuan, Y. Wu, G. Zeng, H. Dong, X. Chen, L. Leng, Z. Wu and L. Peng, *Appl. Catal., B*, 2016, **186**, 19–29.

50 S. Valencia, J. M. Marin, G. Restrepo and F. H. Frimmel, *Water Res.*, 2014, **51**, 124–133.

51 L. Sinatra, A. P. LaGrow, W. Peng, A. R. Kirmani, A. Amassian, H. Idriss and O. M. Bakr, *J. Catal.*, 2015, **322**, 109–117.

52 Y. Shi, Z. Yang, Y. Liu, J. Yu, F. Wang, J. Tong, B. Su and Q. Wang, *RSC Adv.*, 2016, **6**, 39774–39783.

53 Y. Cheng, Y. Lin, J. Xu, J. He, T. Wang, G. Yu, D. Shao, W.-H. Wang, F. Lu, L. Li, X. Du, W. Wang, H. Liu and R. Zheng, *Appl. Surf. Sci.*, 2016, **366**, 120–128.

54 Z. Zhang, K. Liu, Y. Bao and B. Dong, *Appl. Catal., B*, 2017, **203**, 599–606.

55 Z. Li, J. Liu, D. Wang, Y. Gao and J. Shen, *Int. J. Hydrogen Energy*, 2012, **37**, 6431–6437.

56 S. Meng, X. Ning, T. Zhang, S. F. Chen and X. Fu, *Phys. Chem. Chem. Phys.*, 2015, **17**, 11577–11585.

57 C. Li, S. Wang, T. Wang, Y. Wei, P. Zhang and J. Gong, *Small*, 2014, **10**, 2783–2790.